

A High-Resolution Rotation Curve of NGC 6822: A Test-case for Cold Dark Matter

D.T.F. Weldrake,¹ W.J.G. de Blok^{2*}, F. Walter^{3†}

¹ *Research School of Astronomy & Astrophysics, Mount Stromlo Observatory, Cotter Road, Weston Creek, ACT 2611, Australia*

² *Australia Telescope National Facility, PO Box 76, Epping NSW 1710, Australia*

³ *California Institute of Technology, Astronomy Department 105-24, Pasadena, CA 91125, USA*

31 October 2018

ABSTRACT

We present high resolution rotation curves of the local group dwarf irregular galaxy NGC 6822 obtained with the Australia Telescope Compact Array. Our best curves have an angular resolution of $8''$ or 20 pc and contain some 250 independent points. The stellar and gas components of NGC 6822 cannot explain the shape of the curve, except for the very inner regions, and NGC 6822 is consequently very dark matter dominated. There is no evidence for the presence of a steep density cusp down to scales of ~ 20 pc, contrary to the predictions of Cold Dark Matter.

Key words: galaxies: individual (NGC 6822) - galaxies: dwarf - galaxies: fundamental parameters - galaxies: kinematics and dynamics - Local Group - dark matter

1 INTRODUCTION

NGC 6822 is a dwarf irregular local group member. Located at a distance of 490 ± 40 kpc (Mateo 1998), NGC 6822 is the most nearby dwarf irregular apart from the LMC/SMC system. Due to the small distance the galaxy appears very extended on the sky: its optical angular diameter is over a quarter of a degree; the HI disk measures close to a degree (de Blok & Walter 2000). NGC 6822 is a member of an extended cloud of irregulars (Mateo 1998) known as the “Local Group Cloud”. The galaxy has a total luminosity of $M_B = -15.8$ (Hodge et al. 1991) and a total HI mass of $1.3 \times 10^8 M_\odot$ (de Blok & Walter 2000), making it relatively gas-rich. It is a metal poor galaxy, with an ISM abundance of about $0.2 Z_\odot$ (Skillman et al. 1989) and has a star formation rate of $\sim 0.06 M_\odot \text{yr}^{-1}$ (based on H α and FIR fluxes) (Mateo 1998; Israel et al. 1996). Hodge (1980) found evidence for increased star formation between 75 and 100 Myr ago, while Gallart et al. (1996) showed that the star formation in NGC 6822 increased by a factor of 2 to 6 between 100 and 200 Myr ago. This is consistent with the mostly constant but stochastic recent star formation histories often derived for dwarf and LSB galaxies (Grebel 2001; Gerritsen & de Blok 1999). NGC 6822 can be regarded as a rather average and quiescent dwarf irregular galaxy.

de Blok & Walter (2001) found that the outer HI disk is dominated by what appears to be a super-giant HI shell with extended, apparently tidal features in the outer disk. In contrast, the inner main HI disk is remarkably uniform and circularly symmetric. There is no evidence for large kinematical disturbances, as we will show in this paper.

In this paper we address the detailed dynamics and kinematics of NGC 6822 and derive high-resolution rotation curves of this dwarf galaxy. The physical resolution of our highest resolution curve is ~ 20 pc or $\sim 0.03h$ where h is the exponential scale length of the stellar disk (see Sect. 6.1), making it the highest resolution HI rotation curve of any undisturbed dwarf galaxy.

In Section 2 we summarize the “small-scale crisis” in current cosmological simulations. Section 3 briefly describes the observations and data reduction, while Sect. 4 and 5 describe the derivation and analysis of the rotation curves in detail. In Section 6 we describe the models used in rotation curve fitting, while Section 7 presents the results. Section 8 discusses the results, and tries to fit them in the CDM picture. We summarize our conclusions in Section 9.

2 DARK MATTER IN DWARFS

Cosmological numerical Cold Dark Matter (CDM) simulations predict a specific and universal shape for the dark matter mass density distributions (and therefore the rotation curves) of galaxies (Dubinski & Carlberg 1991). This was investigated in detail by Navarro, Frenk & White (1996, 1997) who found that the mass-density distribution in the inner

* Present Address: Department of Physics and Astronomy, Cardiff University, Queen’s Buildings, PO Box 913, Cardiff CF24 3YB, United Kingdom

† Present Address: NRAO AOC, P.O. Box O, 1003 Lopezville Road, Socorro, NM 87801-0387, USA

parts of simulated CDM halos could best be described by a r^{-1} power-law. This steeply increasing density cusp towards the center naturally translates into a steeply rising rotation curve. This kind of curve is however not observed in late-type disk galaxies (e.g. Swaters 1999; Verheijen 1997). The rotation curves of dwarf and Low Surface Brightness (LSB) galaxies are shallow and rise linearly, more consistent with a dark matter distribution that is dominated by a constant-density core with a size of a few kpc (Moore 1994; de Blok & McGaugh 1997; de Blok et al. 2001b; Blais-Ouellette, Amram & Carignan 2001). Especially in the case of LSB galaxies there has been much discussion about the reality of the observed shallow curves (Swaters, Madore & Trehella 2000). It was argued that systematic resolution effects (“beam-smearing”) could hide the steep CDM curves and lead to an erroneous conclusion that they would not be consistent with CDM.

Subsequent high-resolution follow-up studies, measuring the rotation curves of LSB galaxies in H α at a resolution of ~ 0.2 to ~ 1 kpc have now confirmed the conclusions derived from the early data (de Blok et al. 2001b; McGaugh, Rubin & de Blok 2000; de Blok et al. 2001a; de Blok & Bosma 2001; Blais-Ouellette, Amram & Carignan 2001; Bolatto et al. 2002). Dwarfs and LSB galaxies seem to be dominated by a dark matter distribution that is best described in the inner parts by a powerlaw $\rho \sim r^\alpha$ with $\alpha = -0.2 \pm 0.2$ (de Blok et al. 2001b).

With a spatial resolution of only ~ 20 pc, the current data set enables us to measure the rotation curve of this dwarf galaxy at a resolution which is an order of magnitude better than the observations described above. Among other things, the high resolution makes it possible to investigate the effect beam size has on mass models and test whether the inferred distribution of dark matter depends on resolution.

3 OBSERVATIONS AND DATA REDUCTION

NGC 6822 was observed with the Australia Telescope Compact Array for 15×12 hours in its 375 (1×12 h), 750D (2×12 h), 1.5A (4×12 h), 6A and 6D (8×12 h) configurations over the period from June 1999 to March 2000. A total of 8 pointings was observed covering the entire HI extent of the galaxy. We used a bandwidth of 4 MHz with a channel separation of 0.8 km s^{-1} . Additionally, to obtain zero-spacing information, NGC 6822 was observed with the Parkes single dish radio telescope using the multibeam receiver in its narrowband mode in December 1998. The correlator configuration was identical to that used for the Compact Array observations.

The data were reduced and mosaicked together using the MIRIAD data reduction package. Super-uniform weighting, reducing side lobes in individual pointings prior to mosaicing, was used. The resulting data cubes were cleaned with the MIRIAD MOSSDI task. We combined the single dish and synthesis data to correct for the missing zero-spacings and produced data cubes at various spatial and velocity resolutions. For the rotation curve analysis presented here we use the data cubes with channel separations of 1.6 km s^{-1} (with an effective velocity resolution of 1.9 km s^{-1}). These cubes gave the best compromise between velocity resolution and signal-to-noise.

We analyzed the 1.6 km s^{-1} data at five different spatial resolutions. The synthesized beam sizes used were $96'' \times 349.4''$, $48'' \times 174.7''$, $24'' \times 86.4''$, $12'' \times 42.4''$ and $8'' \times 28.3''$. The position angle of the beam was 0° at all resolutions. We will refer to the 5 different resolution data sets as B96, B48, B24, B12 and B08, respectively. Table 1 gives some more information on the data sets. We retained the elliptical beamshape to obtain the highest possible resolution along the major axis. As the PA of the major axis of NGC 6822 is $\sim 110^\circ$, as shown later, this means that the resolution along the major axis is to a few percent equal to the minor axis beam size. The large size of the galaxy compared to the beam rules out any beam smearing effects due to non-major axis information entering the beam.

4 MOMENT MAPS AND VELOCITY FIELD

All subsequent analysis was done using the GIPSY package. The low-resolution cube B96 was clipped at the 2σ level, and remaining noise peaks were removed by hand. Then for B48 and subsequent resolutions, we used the 2σ -clipped cube of the previous resolution as a mask, after which remaining spurious noise peaks were removed by hand. This ensures a consistent selection of features at all resolutions. Furthermore using the lower resolution cube as a mask ensures that possible extended low-level structures are retained in the map.

The integrated HI surface density maps were made in the usual manner by adding together all clipped channel maps. As a second step we then isolated the high signal-to-noise (S/N) regions of the maps as follows. For uniformly tapered maps in velocity $\sigma_{tot} = \sqrt{N}\sigma_{ch}$, where σ_{tot} is the noise in a pixel in the integrated column density map, N is the number of channels contributing to that pixel, and σ_{ch} is the noise in one channel at that pixel. We constructed noise maps for each integrated column density map, and used these together with the column density maps to isolate those pixels in the column density maps where $S/N > 10$. These high S/N maps were used as masks for the velocity fields. Figure 1 shows the integrated column density map derived for the B12 data.

There are two standard ways to produce a velocity field. One commonly used procedure is to determine the intensity weighted mean of the velocities along each profile. It is known that this method can produce spurious velocities at low resolution and low S/N ratios. Given the high resolution and S/N of our data set, this is unlikely to be a problem here. An alternative method is to fit (a) Gaussian(s) to each profile. The latter method usually gives better results, as it is less affected by systematic effects due to skewed profiles etc. It is however computationally more expensive which becomes important for data cubes of the size we are dealing with here. The high quality of the current data puts us firmly in the regime where the intensity weighted mean gives accurate results.

To test this we have compared both methods for the B12 data set (Fig. 2) and find that for our data the differences are negligible. A histogram of the differences is very well described by a Gaussian with an average of -0.3 km s^{-1} and an RMS of 1.0 km s^{-1} , i.e., both methods produce identical results to within better than a channel spacing. The number

of pixels where the residuals reach 5 km s^{-1} or higher is only ~ 0.1 percent of the total number of pixels.

Figure 3 shows a major axis position velocity diagram of the B12 data, taken along a position angle of 120° . Overplotted are the velocities as found in the intensity weighted and Gaussian velocity fields. The velocity fields produce the same results, without large-scale systematic deviations. We will therefore proceed to use intensity weighted velocity fields in subsequent analysis

5 DERIVING ROTATION CURVES

The rotation curves were produced using the GIPSY task ROTCUR. For a well-resolved and high S/N data set such as the current one, the tilted ring procedure is by far the best way to determine the rotation curve. Other methods which are often used, such as adjusting the tilted ring parameters by hand using position velocity diagrams as a guide (e.g. using the GIPSY command INSPECTOR), are more subjective and results can depend on guesses on e.g. the magnitude and effects of beam smearing.

A look at Fig. 2 shows that the high-resolution velocity fields contain an extra-ordinary amount of detail. To get a good feel for the large scale structure in NGC 6822 we started by deriving the B96 rotation curve, and used the results for each resolution as the initial estimate for the next higher resolution, thus gradually refining the curve.

We adopted rings with a width of equal to the minor axis of the beam. The beam is elongated roughly along the minor axis of NGC 6822 with an effective radius of ~ 1.9 times the minor axis. A ring width equal to the minor axis is a good compromise between beam shape and complete sampling. Most information contributing to the rotation curve comes from near the major axis where the beam is narrow.

In general the procedure involved making a fit with all parameters (systemic velocity, centre position, position angle [PA], inclination and rotation velocity) free. The central position and systemic velocity were then fixed and several runs with either inclination or PA or both fixed were made to find the best model.

As the minor axis generally provides little information regarding the rotation curve we excluded an angle of 30° around the minor axis from the fits. One usually also down-weights the data around the minor axis by applying a $|\cos \theta|$ weighting, where θ is the angle with respect to the major axis in the plane of the galaxy. Other alternatives are to apply a uniform weighting or a $\cos^2 \theta$ weighting. We have experimented with different weighting schemes as well as varying the exclusion angle around the minor axis between 15° and 45° , but found no difference in the curves produced (this is due to the large number of independent points that *do* contribute at full weight around the major axis). We therefore adopt a uniform weighting scheme and a free angle around the minor axis of 30° .

Once a satisfactory curve using both sides of the velocity field was produced, we also calculated two curves using only the approaching and receding sides of the velocity field. Comparing the three curves gives information about the symmetry of the system.

5.1 The rotation curves

For each resolution we derived the curve using the procedure described above. The results are shown in Table 2 and Fig. 4. The trends found in PA and inclination for the different resolutions agree well with each other. Only the B96 data does not show the PA trend as strongly. The variation of inclination with radius is only small; only the highest resolutions show weak evidence of a slight warp in the outer parts: choosing a constant inclination instead therefore does only marginally affect the curves. The trend in PA is pronounced and real; deriving curves with a constant PA results in velocities and inclinations that are inconsistent with the data, especially at the higher resolutions. The small-scale kinks in the inclination are not physical and mainly due to dispersion effects.

Beyond $R \sim 1000''$ (2.5 kpc) the difference between the approaching and receding sides becomes more pronounced with increasing resolution. This radius corresponds to the edge of the inner HI disk. The receding curve shows no significant features there, but the approaching curve shows a dip in velocity. This coincides with the interface between the main HI disk and the NW cloud (de Blok & Walter 2001). However, at larger radii the receding curve converges with the approaching one, indicating that the galaxy and cloud (NW side) as well as the “tails” (SE side) are embedded in one symmetrical halo. The global dynamics of the system appear undisturbed despite the morphology of the HI. The small kink at $R \sim 150''$ (0.38 kpc) is caused by a number of high velocity dispersion regions that over a small radial range happen to be aligned with the tilted rings. At $R \sim 500''$ a similar small kink corresponds with the inner edge of the large hole.

Figure 5 shows an overlay of the rotation curve on various position-velocity slices. The rotation curve is a good representation of the dynamics of the galaxy as a whole.

For all resolutions we have compared the velocity fields with model velocity fields constructed from the tilted ring fits, and find no systematic large scale residuals. Figure 6 compares the B12 velocity fields. There are only a few localised regions of slightly higher residuals in the higher resolution models, coinciding with regions of high velocity dispersion. Other resolutions give similar results.

5.2 Final curves

The error-bars derived from the tilted ring fits are an indication of the scatter in velocity around the best-fitting velocity at each tilted ring. As such they do not take into account large-scale asymmetries, differences between approaching and receding sides etc. To define more realistic errors, we regard the absolute difference between the rotation velocities of the approaching and receding sides as 2σ errors. We adopt the maximum of the tilted ring uncertainties and the asymmetry uncertainties as our error-bars, with one further modification. In some cases both sides of the galaxy are very symmetrical, and these usually are also the radii where the tilted ring uncertainties are very small. These combine to give very small errors ($\ll 0.1 \text{ km s}^{-1}$). We have therefore imposed a minimum error of half a channel width on the curves. After corrections for inclination this translates in a minimum error of 0.8 km s^{-1} .

In principle the HI rotation curves also need to be corrected for the pressure gradients in the gas to derive the true rotation velocities. This correction for asymmetric drift is given by

$$v_c^2 = v_\phi^2 - \sigma^2 \left(\frac{\partial \ln \rho}{\partial \ln R} + \frac{\partial \ln \sigma^2}{\partial \ln R} \right),$$

where v_c is the true rotation velocity, v_ϕ the observed gas rotation velocity, σ the velocity dispersion in the gas, and ρ the volume density. The median (modal) velocity dispersion in the disk of NGC 6822 is ~ 5.8 (~ 5.7) km s^{-1} , as measured in the 1.6 km s^{-1} channel spacing data, and does not show any obvious radial trends. Assuming a constant scale height, we can derive the correction for asymmetric drift. We consider the B08 curves where, due to the large gradients in the HI surface density, the corrections are largest. The corrected and uncorrected curves are shown in Fig. 7. Both curves are very similar, with the largest corrections of about $\sim 3 \text{ km s}^{-1}$ occurring between $850''$ and $1050''$. It should be kept in mind that the correction itself is also uncertain and depends on assumptions of e.g. constant scale height, which may not hold in the outer parts of the gas disk. As the uncertainties due to asymmetric drift in the inner parts are negligible, ignoring them will not affect the results. Based on this analysis, we decided not to apply this correction.

5.3 Dynamical centres

The central position as derived above varies slightly from resolution to resolution. This is understandable given the different beam sizes. Fig. 8 shows the central positions over-plotted on a B12 column density map of NGC 6822, where the error-bars span the major and minor axis FWHM of the respective beams. Also plotted are K -band 2MASS (see below) and R -band isophotal centers. Due to the large size, low galactic latitude and the irregular morphology the optical center in NGC 6822 is difficult to determine. From different fits performed at various isophotal levels we estimate an uncertainty of $\sim 0.5'$. These positions are offset from the dynamical center by about $105''$ or 0.25 kpc .

Though the dynamical center is *by definition* the zero-point of the rotation curve, it is instructive to re-derive the rotation curve under the assumption that the optical center is the true center of the galaxy. This is implicitly assumed in many emission line observations of rotation curves where the optical center of the galaxy is frequently used to line up the slit of the spectrograph. We re-derived the B12 rotation curve fixing the position of the center to that of the optical center. We kept the run of position angle and inclination identical to that in the original model. Fig. 9 over-plots the two curves. The overall shape of the curve is insensitive to the precise position of the center. The small-scale differences are of the same order of magnitude as the differences between the approaching and receding sides of the original curve. One should however not exaggerate the importance of this offset: had NGC 6822 been at a more typical distance of a few tens of Mpc, then the angular size of the offset would only be $\sim 1''$ and would have been unnoticed¹.

¹ As an aside, we refer ahead to the discussion on central mass-

6 MASS COMPONENTS

6.1 Stellar component

We used a mosaic of full-resolution 2MASS K_s images to derive the surface brightness profile of NGC 6822. The orientation parameters and the centers of the tilted ring fits to the velocity fields were used to measure the average surface brightness at each radius. Prior to the ellipse integration bright stars were masked out. The average surface brightness contribution of remaining foreground stars in the field away from NGC 6822 was determined and subtracted from the profile.

The K_s surface brightness of NGC 6822 is low and at large radii the scatter is substantial. At radii beyond $750''$ the signal of the galaxy can no longer be distinguished from the sky background. Fig. 11 shows the azimuthally averaged surface brightness profile, corrected for inclination, determined using the B08 tilted ring parameters. The surface brightness was corrected for Galactic foreground extinction, though this was only a small correction of 0.088 mag in the K -band. We assumed NGC 6822 to be optically thin in K , and only applied a geometric inclination surface brightness correction.

The profile can be well described by an exponential disk. As the outer parts of the profile could be marginally affected by small uncertainties in the sky background we have fitted an exponential disk to the profile at $R < 400''$ and find an exponential scale length of $286''$ or 0.68 kpc . The central surface brightness is $\mu_0^i(K_s) = 19.8 \text{ mag arcsec}^{-2}$. The total absolute magnitude we derive assuming an exponential disk and extrapolating to infinity is $M_K = -17.9$ or $L_K = 3.8 \times 10^8 L_\odot$.

For each resolution we determine the surface brightness profiles using the relevant tilted ring parameters determined. At $R > 240''$ we replace the surface brightness profiles with that of the exponential disk fit as indicated in Fig. 11. The rotation curve of the stellar disk was then computed from the extended K -band profile following Casertano (1993) and Begeman (1987). The disk was assumed to have a vertical sech^2 distribution with a scale height $z_0 = h/6$ (van der Kruit & Searle 1981). The rotation curves of the stellar component were sampled at the same radii as the rotation curves. We assume Υ_* is constant with radius. While one expects some modest variation in Υ_* with radius in optical bands (de Jong 1996), the colour gradients in dwarf LSB galaxies in the K band tend to be small, so this effect is not likely to be significant (see also Sect. 6.4).

6.2 Gas component

We used the orientation parameters of the tilted ring fits to determine the azimuthally average HI surface density profiles using the total column density maps for each resolution.

density slopes in Sect. 8.1, where we determine the power-law slope α of the mass-density profile $\rho \sim r^\alpha$ within a radius of 0.8 kpc . For the B12 case we there find a slope of $\alpha = -0.04 \pm 0.09$. For the curve presented here, determined using the optical center and also using an outer radius of 0.8 kpc , a similar analysis gives $\alpha = -0.23 \pm 0.24$. The uncertainties are larger, but the value is consistent with a soft core in NGC 6822. The exact position of the dynamical center does not significantly influence the results.

The HI surface density profiles are presented in Fig. 10. In deriving the corresponding rotation curve with the GIPSY task ROTMOD we scaled the surface density profiles by a factor of 1.4 to take the contribution of helium and metals into account.

We assume that the gas is distributed in an infinitely thin disk. This assumption is not crucial. Though one might expect dwarf galaxies to have a more puffed up disk than a typical spiral galaxy, the shape and amplitude of the gas rotation curve depends only very mildly on the thickness of the disk.

To use the B12 curve as an example, for the infinitely thin gas disk case the maximum rotation velocity of the gas component is 17 km s⁻¹. When increasing the thickness of the disk, this maximum rotation velocity drops only very slowly: for an exponential scale height $z = 0.5$ kpc, it still measures ~ 14.5 km s⁻¹. This value for z is already approaching the value of the radial scale length of the stellar distribution and likely already too large. We thus adopt the thin disk approximation.

6.3 Halo models

The dark halo component differs from the previous two in that we are interested in parametrising this component assuming some fiducial model. The choice of this model is the crux of most of the DM analyses in the literature, and many models exist. These can all be broadly distinguished in two groups: halo models with a core, and halo models with a cusp. An example of the first category is the pseudo-isothermal halo, an example of the latter the CDM NFW halo.

6.3.1 Pseudo-isothermal halo

The spherical pseudo-isothermal (ISO) halo has a density profile

$$\rho_{ISO}(R) = \frac{\rho_0}{1 + (R/R_C)^2}, \quad (1)$$

where ρ_0 is the central density of the halo, and R_C the core radius of the halo. The corresponding rotation curve is given by

$$V(R) = \sqrt{4\pi G \rho_0 R_C^2 \left[1 - \frac{R_C}{R} \arctan\left(\frac{R}{R_C}\right) \right]}. \quad (2)$$

The asymptotic velocity of the halo, V_∞ , is given by

$$V_\infty = \sqrt{4\pi G \rho_0 R_C^2}. \quad (3)$$

To characterise this halo only two of the three parameters (ρ_0, R_C, V_∞) are needed, as equation (3) determines the value of the third parameter.

6.3.2 NFW halo

The NFW mass density distribution takes the form (Navarro, Frenk & White 1996)

$$\rho_{NFW}(R) = \frac{\rho_0}{(R/r_0)[1 + (R/r_0)]^2} \quad (4)$$

where r_0 is the characteristic radius of the halo and ρ_0 the characteristic density (Navarro, Frenk & White 1996; Blaiz-Ouellette, Amram & Carignan 2001). This mass distribution gives rise to a halo rotation curve

$$V(R) = V_{200} \left[\frac{\ln(1+cx) - cx/(1+cx)}{x[\ln(1+c) - c/(1+c)]} \right]^{1/2}, \quad (5)$$

where $x = R/R_{200}$. It is characterised by a concentration parameter $c = R_{200}/R_s$ and a radius R_{200} . These are directly related to R_s and ρ_i , but are used instead as they are a convenient way to parametrise the rotation curve. The radius R_{200} is the radius where the density contrast exceeds 200, roughly the virial radius (Navarro, Frenk & White 1996). The characteristic velocity V_{200} of the halo is defined in the same way as R_{200} . These parameters are not independent and are set by the cosmology.

6.4 Stellar Mass-to-light ratios and weighting

One of largest uncertainties in any mass model is the value of the stellar mass-to-light ratio Υ_* . Though broad trends in Υ_* have been measured and modelled (e.g. Bottema 1997; Bell & de Jong 2000), the precise value for an individual galaxy is not well known, and depends on extinction, star formation history, Initial Mass Function, etc. The value of Υ_* cannot be constrained using the rotation curve alone (van Albada & Sancisi 1986; Lake & Feinswog 1989) and some assumptions must be made. We therefore present disk-halo decompositions using four different assumptions.

Minimum disk. This model assumes that the observed rotation curve is due entirely to DM. This gives an upper limit on how concentrated the dark mass component can actually be. It is not a realistic model *per se*, because it ignores the gas disk which is obviously present. However, we present it here for ease of comparison with cosmological simulations, a large fraction of which tend to only model the dark matter component.

Minimum disk + gas. The contribution of the atomic gas (HI and He) is taken into account, but Υ_* is assumed to be zero.

Constant Υ_* . Here we choose a value for Υ_* appropriate for NGC 6822 based on its stellar content, colours and likely star formation history. Unfortunately reliable integrated colours for NGC 6822 are rare due to its large angular size. We can however use indirect arguments to arrive at a value for Υ_* . Furthermore we are interested here only in the K -band value which is rather insensitive to effects of extinction and recent star formation.

Verheijen (1997) presents K' -band rotation curve fits of a large sample of HSB and LSB galaxies in the Ursa Major cluster. We consider the rotation curve fits derived using the Bottema disk prescription (Bottema 1997). This recipe states that the maximum rotation velocity of the disk is 63% of the maximum rotation velocity observed (and is derived from measurements of stellar velocity dispersions). The distribution of Υ_{*K} ratios derived with the Bottema disk for the dwarf and LSB galaxies in the UMa sample peaks at $\Upsilon_{*K} = 0.4 \pm 0.05$. If the colours of NGC 6822 are comparable to those found for other dwarfs and LSB galaxies (namely $B - V \sim 0.5$, $B - R \sim 0.8$ and $V - I \sim 0.8$; de Blok, van der Hulst & Bothun 1995) we can use Table 3 in

Bell & de Jong (2000) to derive an approximate value for Υ_* . For their formation epoch model with burst we find values for Υ_{*K} between 0.35 and 0.40. Similar values are found for the infall models and the hierarchical models. From detailed population synthesis modelling of NGC 6822, Gallart et al. (1996) find that the total mass of stars and stellar remnant ever formed in NGC 6822 must be $\sim 9 \cdot 10^7 M_\odot$. Combined with the K -band luminosity derived earlier, this gives a value $\Upsilon_{*K} = 0.24$.

Taking the above into account we adopt a value of $\Upsilon_{*K} = 0.35$ as representative of the stellar population in NGC 6822.

Maximum disk. The rotation curve of the stellar component is scaled to the maximum value allowed by the observed rotation curve, but with the restriction that the DM density gradient is required to be flat or negative at all radii (thus avoiding a “hollow halo”) (van Albada & Sancisi 1986).

Each of the rotation curves was fitted using the GIPSY task ROTMAS. The program determines the best-fitting combination of R_C and V_∞ (for the pseudo-isothermal halo) or c and V_{200} (for the NFW halo), using a least squares fitting routine. We assigned weights to the data points inversely proportional to the square of their uncertainty.

7 RESULTS

Figures 12-16 show the rotation curves at all resolutions plotted for the four assumptions on Υ_* for both NFW and ISO halo models. To rule out the possibility that the outer parts of NGC 6822, which might be affected by tidal effects, affect our conclusions we also present separate fits to just the inner part of the galaxy out to $R = 1000''$ (2.4 kpc) or the edge of the main inner disk. Tables 3 and 4 present the fit parameters for all models presented here.

An inspection of Tables 3 and 4 shows that the goodness-of-fit is in all cases better for ISO than for NFW. The only exceptions are some of the maximum disk fits where both ISO and NFW are difficult to fit, as NGC 6822 is not a maximum disk galaxy. A comparison between the χ^2 values is shown in Fig. 17.

The maximum disk values of Υ_* generally have an uncertainty of $\pm \sim 0.1$. Changing the values within this range has no discernible effect on the quality of the fits. One point of note is that for the B08 case the maximum disk value for Υ_* is less than that for the constant Υ_* case. The B08 constant Υ_* fit thus results in a hollow halo.

Many of the NFW fits have fit parameters that do not make physical sense. The large majority of the fits prefer $c \leq 0$ and $V_{200} \rightarrow \infty$, which is another way of saying that the fit procedure is trying to fit a $V \sim R^{1/2}$ curve to a $V \sim R$ curve by stretching it to infinity, thus trying to take out the curvature in the model. Where this happened we fixed the c parameter to $c = 0.1$ with only V_{200} as the free parameter. Such a value is still outside the range predicted by cosmological simulations where values of $c \sim 10$ would be expected. There is a general trend for the value of the maximum disk Υ_* to decrease with increasing resolution. It is not clear what the cause of this effect is. The inner slopes of the rotation curve and stellar curve change subtly with resolution, but not enough to be the sole cause. It is likely

that small differences between the tilted ring models also play a role.

We note that at all resolutions we find that (restricting ourselves to the ISO model for a moment) the min+gas model usually has the smallest value of χ^2 , and that for all cases $\chi_{m+g}^2 < \chi_{con}^2$. We have tried to constrain the value of Υ_* by making a “best fit” to the rotation curves using ISO models: i.e. we also let Υ_* be a free parameter in the fits. Unfortunately the different resolutions make it difficult to constrain Υ_* in this manner. The B96 data is best fitted with a stellar component with $\Upsilon_{*K} = 0.10 \pm 0.13$, while the B48 and B24 curves both demand $\Upsilon_{*K} = 0.31 \pm 0.04$. For the B08 and B12 data such a “best fit” gives unphysical results (negative Υ_*). A constrained fit with $\Upsilon_* \geq 0$ yields $\Upsilon_* = 0$ (i.e. the minimum disk+gas case) as best fit for these resolutions. Though it is clear that Υ_* is difficult to constrain using only rotation curve information, the results do suggest that the stellar population is dynamically unimportant.

8 DISCUSSION

8.1 Inner slopes

With the high-resolution rotation curves we can determine the inner slope of the mass-density distribution. The rationale behind this is described in de Blok et al. (2001b). In summary, the various halo models make specific predictions about the slope of the dark matter mass density distribution in the inner parts. If we approximate this distribution with a power-law $\rho \sim r^\alpha$, then the ISO halo predicts $\alpha = 0$, while the NFW halo predicts $\alpha = -1$. In de Blok et al. (2001b) the inner mass density slopes of a large sample of LSB galaxies was derived, and the most representative value was $\alpha = -0.2 \pm 0.2$, i.e. closer to pseudo-isothermal than to CDM.

Here we derive the slopes of the mass density distribution of NGC 6822 at various resolutions using the inversion method described in de Blok et al. (2001b) where we compute the mass density profile and fit a power-law to the mass-density profile. Fig. 18 shows two examples. We show the B96 and B24 mass-density profiles, with the best fitting NFW and ISO (minimum disk) models over-plotted. The NFW models have central densities that are discrepant by a factor of 10 or more.

We measure the slope within $R = 0.8$ kpc. This is an arbitrary choice, motivated by the fact that we want to use at least 3 data points to determine the slope of the B96 curve. Other choices are obviously possible, and may result in slightly different values of the slope, but will not affect the conclusions. The resulting values are given in Table 5. For the B08 data a meaningful slope could not be derived due to the large gradients in the rotation velocity that are found at small scales. The values are at all resolutions significantly different from the NFW values. Note that there is no systematic steepening of the slope with resolution, which one would expect if the cusp was hidden by resolution effects. With a resolution of only tens of parsecs it is not clear that there is still room for a cusp in NGC 6822.

8.2 Dark matter, feedback and cosmology

In the previous sections we have made NFW fits to the rotation curves disregarding any of the predictions that CDM makes for c , V_{200} and their relation. We will compare the observed rotation curve with cosmological predictions. If we assume that $V_{200} \simeq V_{\max} \simeq 55 \text{ km s}^{-1}$, we find for Λ CDM that $c \simeq 9.5$ (Navarro, Frenk & White 1997). The total mass M_{200} of this halo is $M_{200} = 5.2 \cdot 10^{10} M_{\odot}$. This predicted halo is over-plotted on the observed curve in Fig. 19, and over-predicts the rotation velocity in the inner parts by a significant amount.

To look at the problem from a different perspective, let us assume $\Upsilon_{*}=0.35$. This gives a stellar mass $M_{*} = 1.3 \times 10^8 M_{\odot}$. The total (atomic) gas mass is $1.5 \times 10^8 M_{\odot}$ (HI+He) and the total observed baryonic mass is $2.8 \times 10^8 M_{\odot}$. A universal baryon fraction of ~ 0.09 (see e.g. White & Fabian 1995) implies a total mass $M_{200} = 3.1 \times 10^9 M_{\odot}$. For a NFW halo this implies $V_{200} = 21.5 \text{ km s}^{-1}$ and $R_{200} = 28 \text{ kpc}$. These values are not consistent with the observed curve, and imply (apart from the inability of the model to fit the data) that either the baryon fraction in NGC 6822 differs significantly from the universal value or that large amounts of baryons have been expelled, as we will discuss below in more detail.

Let us work out the *observed* matter fractions in NGC 6822. We use the ISO models, and determine the amount of dark matter within a radius of 5 kpc, the outer edge of the HI disk. This yields a total dark mass out to 5 kpc of $3.2 \times 10^9 M_{\odot}$. With an observed baryonic mass of $2.8 \times 10^8 M_{\odot}$ we find that NGC 6822 is heavily dark matter dominated with $M_{\text{vis}}/M_{\text{dark}}(R < 5\text{kpc}) = 0.09$. This is comparable to values found in LSB galaxies and other dwarf galaxies (de Blok & McGaugh 1997). The corresponding baryon fraction is $f_b = 0.080$, close to the universal baryon fraction.

The visible matter in NGC 6822 is thus a minor component of the total galaxy system. This makes it harder to explain the observed core-dominated dark matter distribution as resulting from a NFW halo modified by feedback. The term feedback is often used indiscriminately to indicate star formation and evolutionary processes that affect the mass distribution in a galaxy. In fact, there are two distinct forms of feedback. One of them is commonly observed in galaxies, also in NGC 6822, and usually shows itself as small-scale redistribution of mass in the disk.

The second form of feedback is more catastrophic, mostly theoretical, and was introduced to explain the discrepancy between observed and theoretical dark matter distributions. In essence it invokes large-scale and violent star formation, resulting in massive blow-outs that drag dark matter out due to gravitational interactions, thus destroying the primordial CDM cusp. The exact physics of feedback are not understood, and the models usually resorts to an empirical description that is fine-tuned to e.g. fit the Tully-Fisher relation or other observational constraints.

Nevertheless, let us explore the implications of feedback: using the amount of energy produced by supernovae and making some standard assumptions one can work out an expression for the amount of matter expelled by the effects of supernovae (see e.g. Eq. (A4) in van den Bosch et al. 2000). Feedback then requires the baryonic mass to drag along a

similar amount of dark matter (modulo some efficiency factor that is unlikely to be much larger than unity).

Assuming CDM halos, we find for $V_{200} \simeq 55 \text{ km s}^{-1}$ that $M_{200} = 5.2 \times 10^{10} M_{\odot}$. Equation A4 in van den Bosch et al. (2000) then yields that the expelled baryonic mass is $3.6 \times 10^9 M_{\odot}$. Assuming that the efficiency factor is unity (every unit mass of baryons drags along one unit mass of dark matter) we find that the amount of dark matter relocated is about equal to the amount of dark matter currently observed within the outermost radius of the observed disk. We are thus dealing with a major structural re-organisation of a galaxy.

Even if we assume the maximum possible maximum disk $\Upsilon_{*}=0.95$ we still only find an observed baryonic mass of $5.4 \times 10^8 M_{\odot}$ (though not physically motivated, this is a hard upper limit on the observed baryonic mass). Assuming an efficiency factor of unity, it seems NGC 6822 must have expelled over ~ 6 times its currently observed baryonic mass.

There has been some discussion in the past whether or not stellar feedback can remove a significant fraction of the mass of a galaxy to the Intergalactic Medium. Gnedin & Zhao (2002), as well as Mac Low & Ferrara (1998) showed that this process is unable to explain the observed cores, and is also inconsistent with other observational constraints. According to numerical simulation of stellar feedback by Mac Low & Ferrara (1998) the potential mass loss is a function of the total galaxy mass; for galaxies with gas masses $< 10^6 M_{\odot}$ a galaxy can potentially destroy itself ('blow-away' scenario) whereas for gas masses between 10^6 and $10^9 M_{\odot}$ some material may be removed ('blow-out', see their Fig. 1). According to these models we do not expect significant mass loss in NGC 6822 ($M_{\text{gas}} = 1.5 \cdot 10^8$) due to violent star formation.

From an observer's perspective, there is relatively little evidence that mass loss does indeed occur in dwarf galaxies. Although strong outflow signatures are observed in some cases in dwarf galaxies there are only few cases where outflow material may permanently escape the galactic gravitational potential (e.g. Martin 1998).

A further problem with expelling a lot of mass are the global dynamics of the galaxy: if one were to have a huge mass loss of order a few times the total galaxy mass, one would certainly expect to find some clear evidence in the velocity field. The blown-out gas is such a case unlikely to end up as an undisturbed regularly rotating HI disk. Furthermore, the stellar record shows no evidence for increases in the SFR with large factors at any time during the past ~ 9 Gyr (Gallart et al. 1996). It thus seems somewhat surprising that if feedback had occurred, it would have managed to hide all traces of a violent past.

In summary, we conclude that potential feedback of several times the total baryonic mass of NGC 6822 is unlikely. The observed rotation curve of NGC 6822, combined with the K -band and HI data thus lead to a picture inconsistent with a combination of cuspy halo and feedback.

9 CONCLUSIONS

We obtained high resolution rotation curves for the local group dwarf irregular galaxy NGC 6822. By fitting both

pseudo-isothermal and NFW halo models, it was found that the pseudo-isothermal model fits the data successfully. NGC 6822 is not maximum disk and is dominated by dark matter. The highest resolution rotation curve has some 250 independent points and beam-smearing effects are not an issue. The position of the dynamical center is unambiguously determined. There is no indication of a dark matter cusp down to scales of ~ 20 pc.

Trying to explain the observed curve with a combination of feedback and CDM halos leads to several inconsistencies. Feedback and CDM seem to imply that NGC 6822 has lost about 6 times the currently observed amount of baryons. There is however no evidence for such violent processes. We therefore conclude that (i) the dark matter distribution in NGC 6822 is unlikely to have been affected by feedback, and (ii) is best described by a model with a constant density core.

ACKNOWLEDGEMENTS

We thank Steve Schneider for providing us with the 2MASS images. We thank Sébastien Blais-Ouellette for constructive comments that helped improve this paper. This publication makes use of data products from the Two Micron All Sky Survey, which is a joint project of the University of Massachusetts and the Infrared Processing and Analysis Center/California Institute of Technology, funded by the National Aeronautics and Space Administration and the National Science Foundation.

REFERENCES

- Bell, E.F., de Jong, R.S., 2000, MNRAS, 312, 497
 Bottama, R., 1997, A&A, 328, 517
 Begeman, K., 1987, PhD Thesis, University of Groningen
 Blais-Ouellette, S., Amram, P., Carignan, C., 2001, AJ, 121, 1952
 Bolatto, A.D., Simon, J.D., Leroy, A., Blitz, L., 2002, ApJ, 565, 238
 Bullock, J.S., Kolatt, T.S., Sigad, Y., Somerville, R.S., Kravtsov, A.V., Klypin, A.A., Primack, J.R., & Dekel, A. 2001, MNRAS, 321, 559
 Casertano, S. 1983, MNRAS, 203, 735
 Bosma, A., de Blok, W.J.G., 2002, A&A, 385, 816
 de Blok, W.J.G., McGaugh, S.S., 1997, MNRAS, 290, 533
 de Blok, W.J.G., Walter, F., 2000, in "Mapping the Hidden Universe: The Universe behind the Milky Way - The Universe in HI." ASP Conference Proceedings, Vol. 218, edited by Renée C. Kraan-Korteweg, Patricia A. Henning, and Heinz Andernach. Astronomical Society of the Pacific, ISBN 1-58381-050-1, 2000, p.357
 de Blok W.J.G., van der Hulst J.M., Bothun G.D., 1995, MNRAS, 274, 235
 de Blok, W.J.G., McGaugh, S.S., Rubin, V., 2001, AJ, 122, 2396
 de Blok, W.J.G., McGaugh, S.S., Bosma, A., Rubin, V., 2001, ApJL, 552, L23
 de Blok, W.J.G., Walter, F., 2001, ApJ, 537, L95
 de Jong, R.S., 1996, A&A, 313, 377
 Dubinski, J., Carlberg, R.G., 1991, ApJ, 378, 496
 Gallart, C., Aparicio, A., Bertelli, G., Chiosi, C. 1996b, AJ, 112, 2596
 Gerritsen, J.P.E., de Blok, W.J.G., 1999, A&A, 342, 655
 Gnedin, O.Y., Zhao, H-S, 2002, MNRAS, 333, 299
 Grebel, E.K., 2001, ApSSS, 277, 231
 Hodge, P.W., 1980, ApJ, 241, 125
 Hodge, P., Smith, T., Eskridge, P., MacGillivray, H., Beard, S. 1991, ApJ, 379, 621
 Israel, F.P., Bontekoe, Tj.R., Kester, D.J.M, 1996, A&A, 308, 723
 Lake, G., Feinswog, L. 1989, AJ, 98, 166
 Mac Low, M.-M., Ferrara, A., 1998, ApJ, 513, 142
 Mateo, M.L. 1998, ARA&A, 36, 435
 Martin, C.L., 1998, ApJ, 506, 222
 McGaugh, S.S., Rubin, V., de Blok, W.J.G., 2000, ApJ, submitted
 Moore, B. 1994, Nature, 370, 629
 Navarro, J.F., Frenk, C.S., White, S.D.M. 1996, ApJ, 462, 563
 Navarro, J.F., Frenk, C.S., & White, S.D.M. 1997, ApJ, 490, 493
 Skillman, E.D., Terlevich, R., Melnick, J. 1989, MNRAS, 240, 563
 Swaters, R.A., 1999, PhD Thesis, University of Groningen
 Swaters, R.A., Madore, B.F., Trewhella, M., 2000, ApJL, 531, L107
 van Albada, T.S, Sancisi, R., 1986, Phil. Trans. R. Soc. Lond. A, 320, 447
 van der Kruit, P.C., & Searle, L. 1981, A&A, 95, 105
 van den Bosch, F.C., Robertson, B.E., Dalcanton, J.J., de Blok, W.J.G., 2000, AJ, 119, 1579
 Verheijen, M.A.W., PhD Thesis, University of Groningen
 White, D.A., Fabian, A.C., 1995, MNRAS, 273, 72

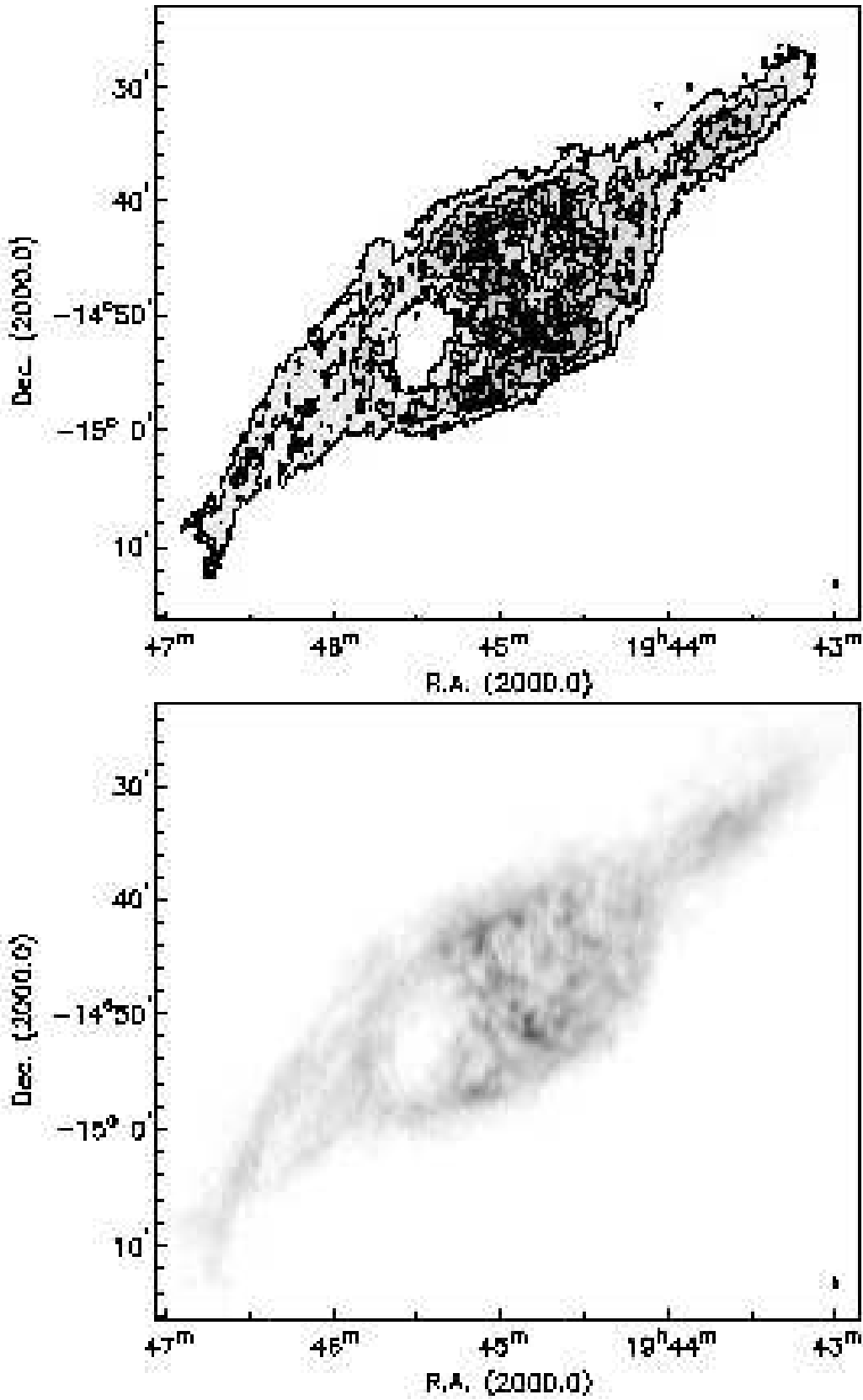


Figure 1. B12 total column density map. Contours start at $5 M_{\odot} \text{pc}^{-2}$ and increase in steps of $1 M_{\odot} \text{pc}^{-2}$. The beam is indicated in the lower right corner.

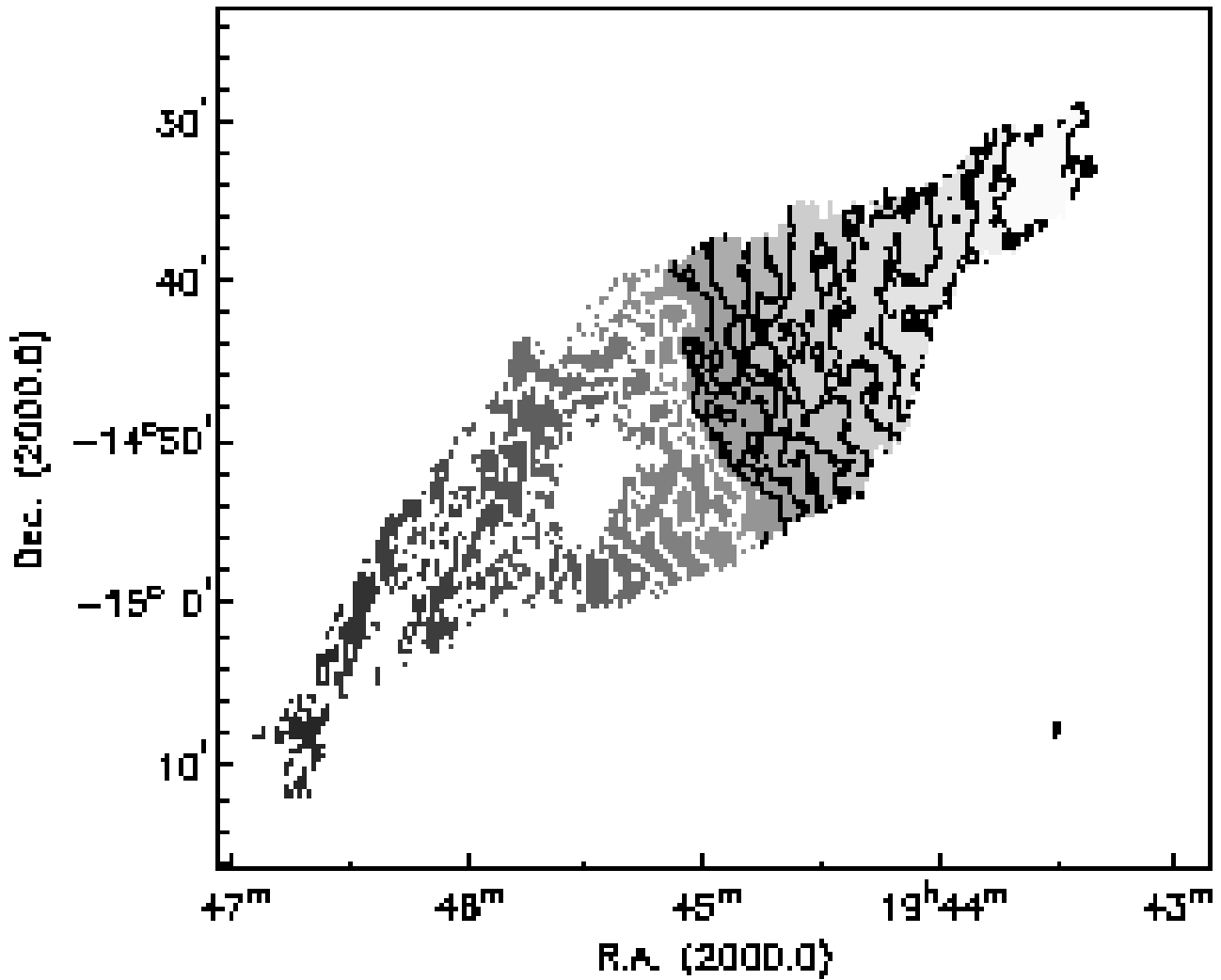


Figure 2. The intensity weighted velocity field, derived from the B12 data. The black contours run from -55 km s^{-1} in the central parts to -100 km s^{-1} in the outer NW parts, in steps of 5 km s^{-1} . The white contours run from -50 km s^{-1} in the inner parts to $+10 \text{ km s}^{-1}$ in the outer SE parts. The beam is shown in the lower-right corner.

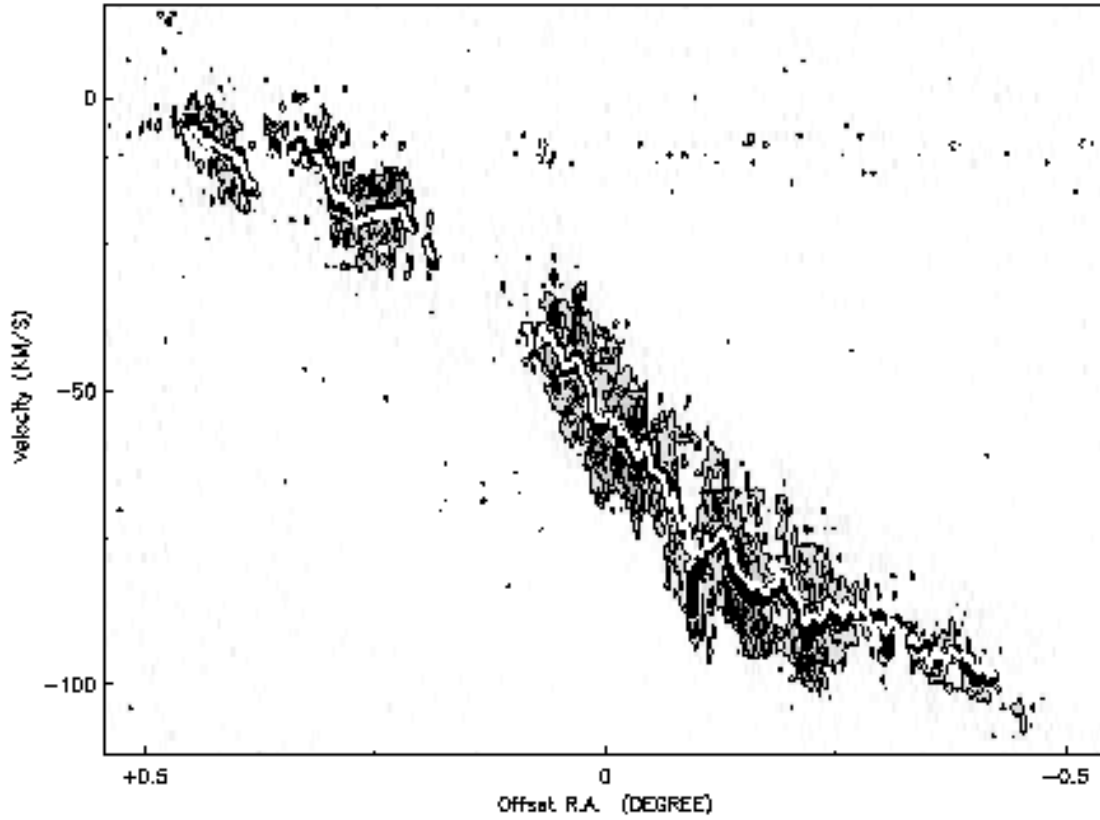


Figure 3. B12 data major axis position-velocity diagram taken along position angle 120° . Dotted contour represents -4σ , full contours start at 4σ and increase in steps of 2σ . The white line shows the values found in the intensity weighted velocity field. The black line shows values derived from the gaussian velocity field.

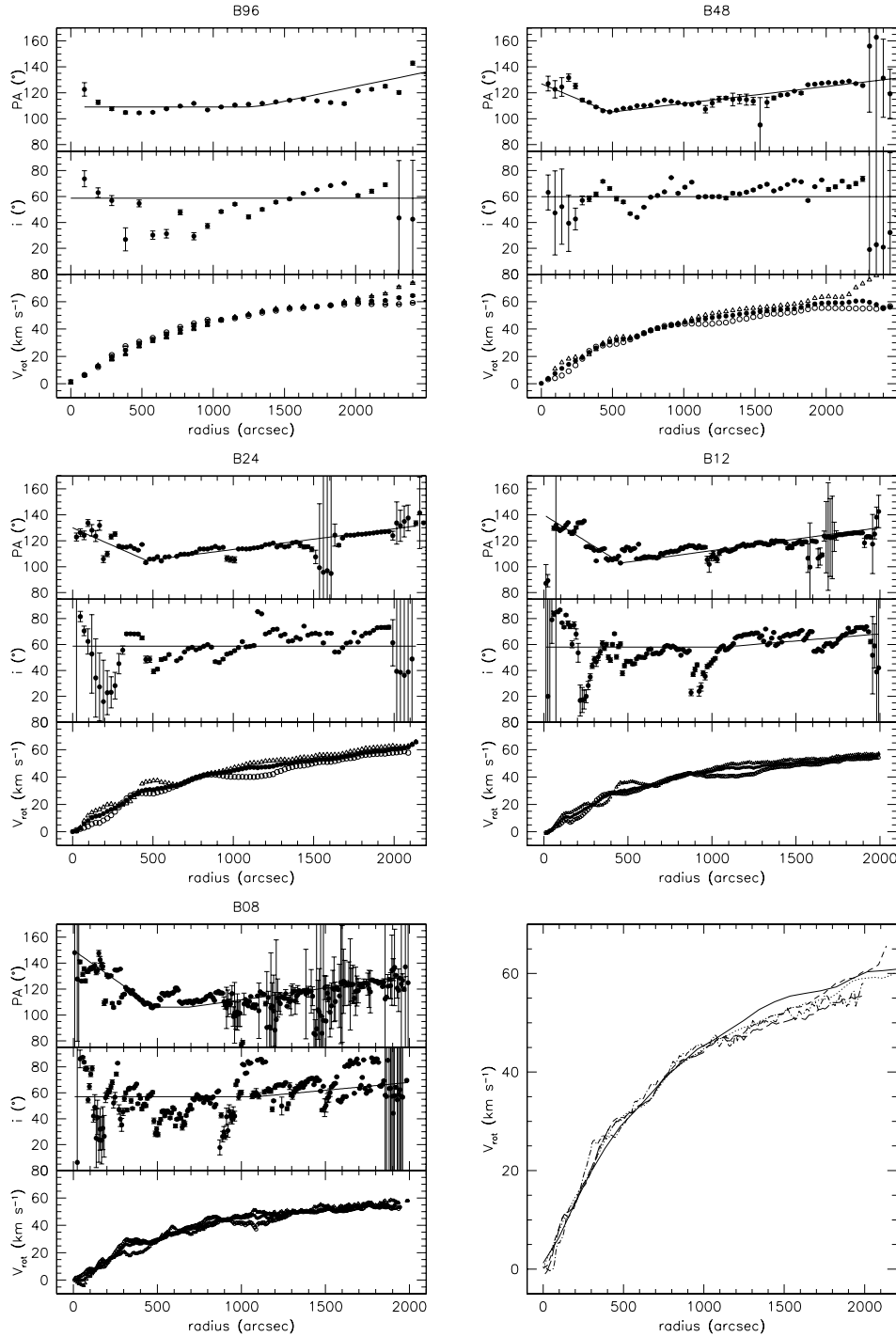


Figure 4. Results of the tilted ring fits for the B96, B48 (top row), B24, B12 (middle row) and B08 (bottom-left) resolutions. In each panel we show the the position angle of the major axis (top), the inclination (centre) and circular velocity (bottom) as a function of radius for the various resolutions. In every top sub-panel the filled circles represent the curve derived using the whole velocity field. The open circles represent the curve for the approaching (SE) side, while the triangles represent the receding (NW) side. Overplotted in the top and centre sub-panels are the models used to derive these curves. The points in the top sub-panel show the behaviour of PA as a free parameter, with inclination fixed to its model value as shown in the center panel. The points in the center sub-panel show the behaviour of inclination with PA fixed to the model values as shown in the top panel. The bottom-right panel shows the rotation curves at each resolution overplotted. Full line: B96; dotted line: B48; short-dashed line: B24; long-dashed line: B12; dash-dotted line: B08.

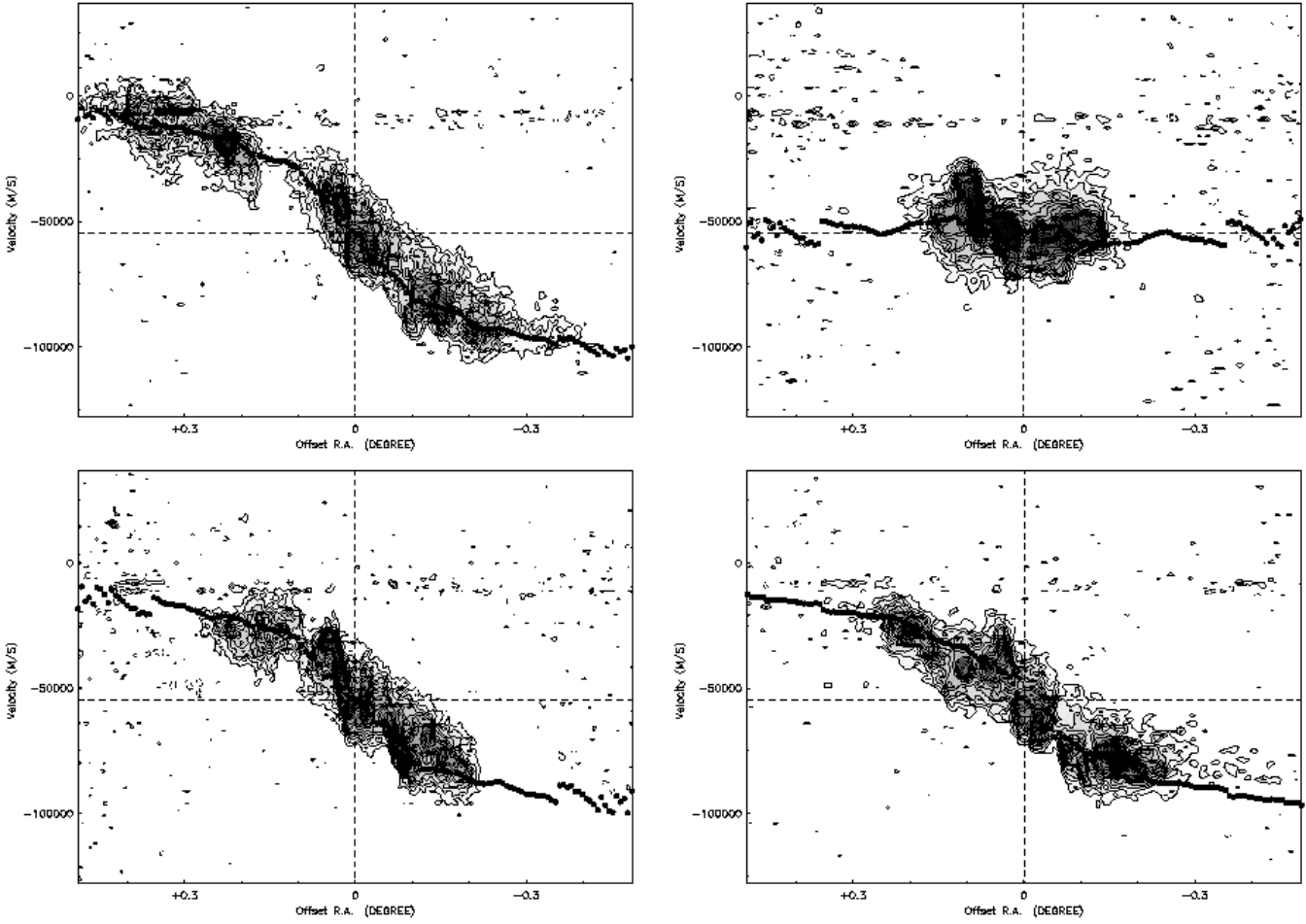


Figure 5. Position velocity slices of the B24 data, with the projected rotation curve overplotted. The full contours are plotted starting at 3σ in steps of 2σ . The dotted contours show the -3σ and -5σ levels. There is residual Milky Way emission present at $\sim -10 \text{ km s}^{-1}$. The dotted lines represent the center of the galaxy and the systemic velocity. Overplotted is the final curve as derived from the tilted ring fits, corrected to the position angle of the slice. Top left: major axis position-velocity slice taken at a position angle of 115° . Top right: minor axis position-velocity slice. Bottom left: position angle of major axis minus 30° . Bottom right: position angle of major axis plus 30° . NGC 6822 is, despite the disturbed morphology, a very symmetrical galaxy.

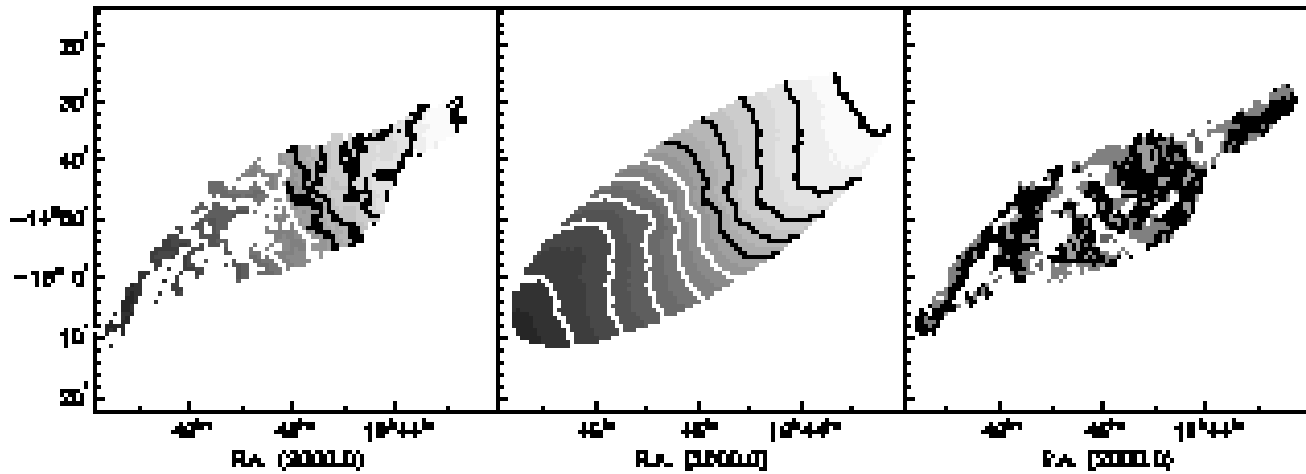


Figure 6. Comparison of the observed velocity fields (left column) and the circularly symmetric model velocity fields derived from the tilted ring fits (centre column). The white velocity contours start in the center of the velocity field at -50 km s^{-1} and increase in steps of 10 km s^{-1} . The black contours start in the centre at -55 km s^{-1} and decrease in steps of 10 km s^{-1} towards the NW. The right most column shows the residual velocity field (observed–tilted ring). The first white contour represents $+5 \text{ km s}^{-1}$ and subsequent white contours increase with a step of 5 km s^{-1} . The first black contour shows the -5 km s^{-1} and subsequent black contours decrease in steps of 5 km s^{-1} .

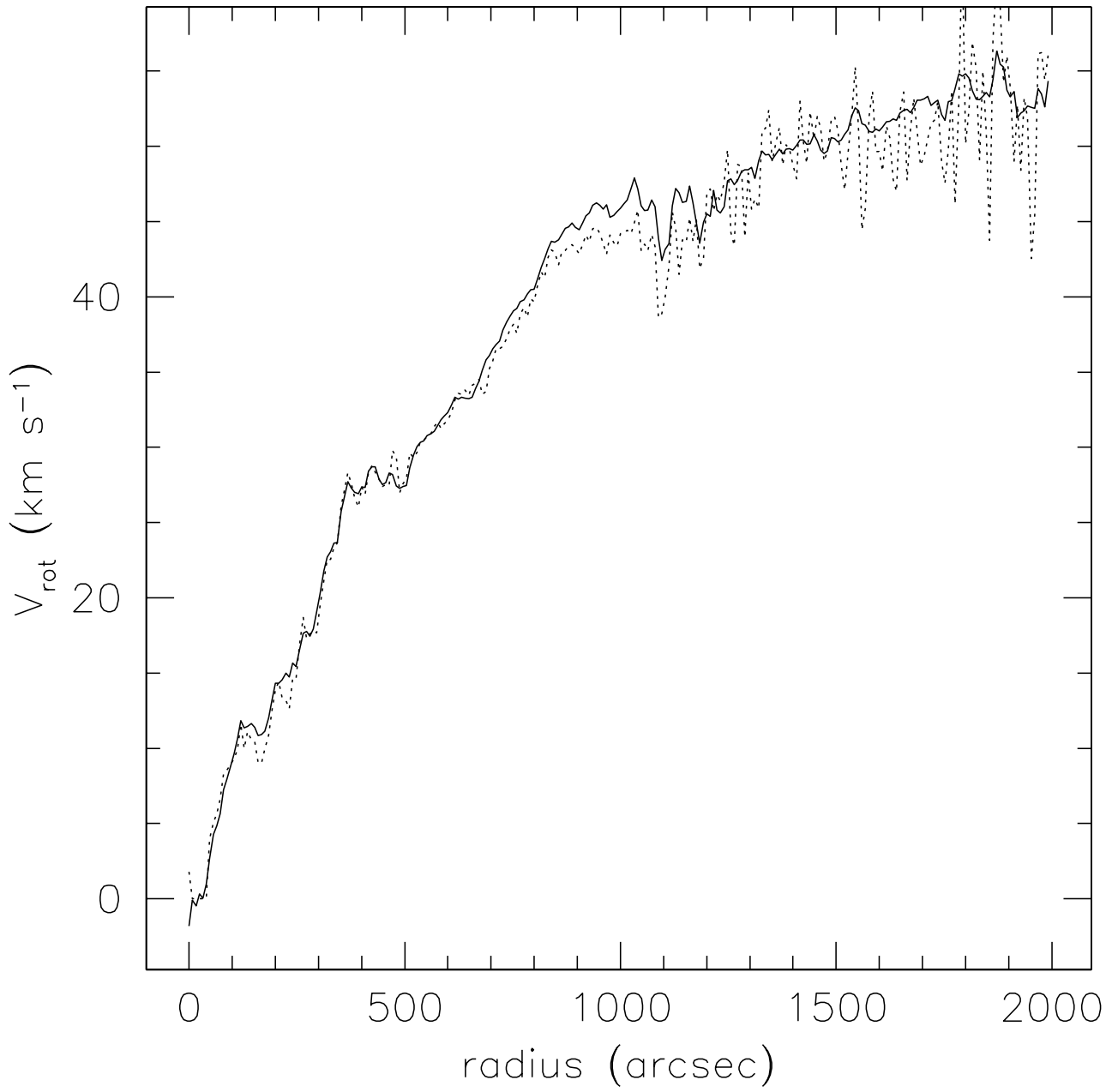


Figure 7. The B08 rotation curve (solid line) and corrected for asymmetric drift (dotted line)

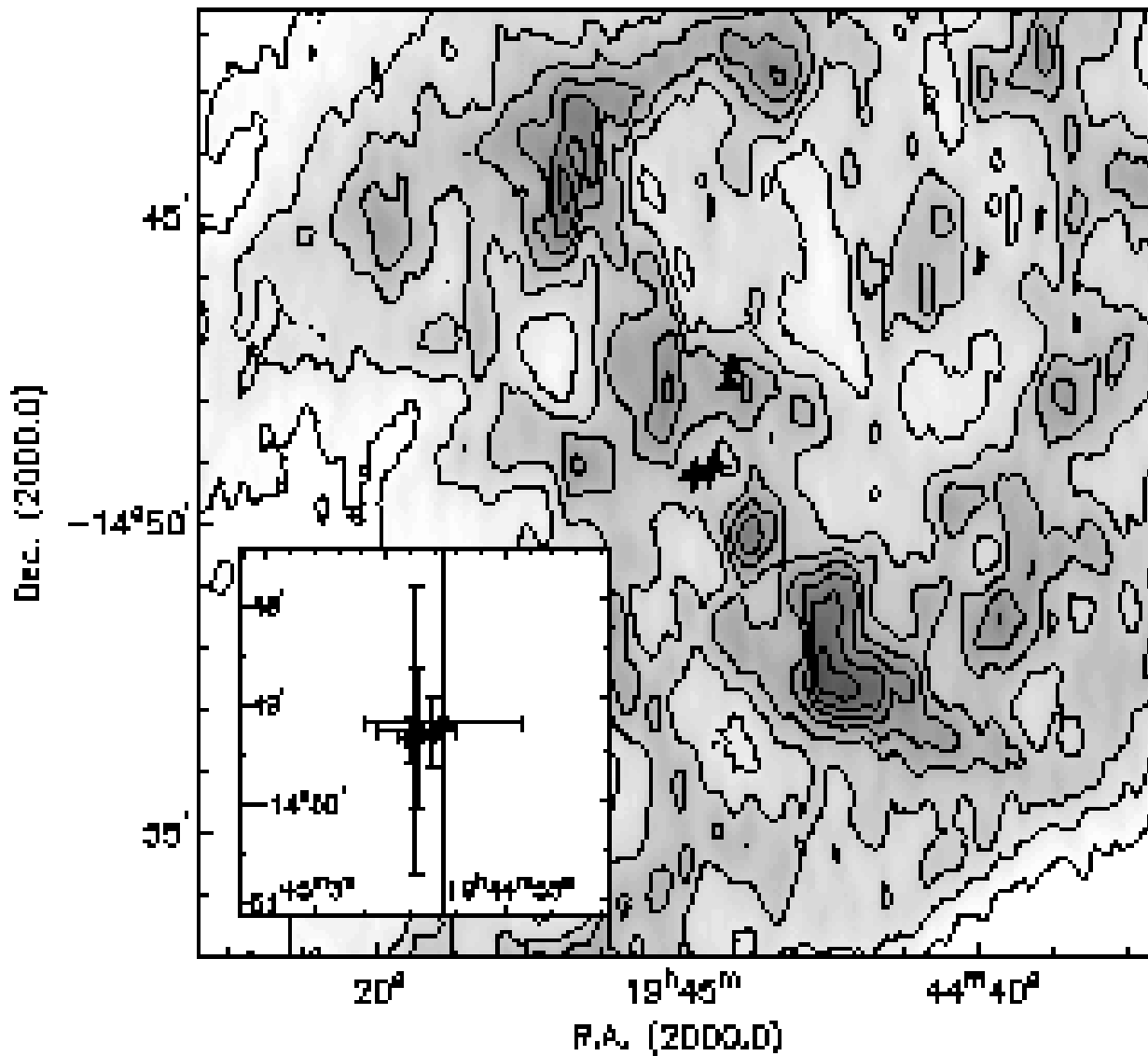


Figure 8. Positions of the dynamical centers of the 5 resolutions (crosses) overplotted on the B12 total column density map. Contours start at $5 M_{\odot} \text{pc}^{-2}$ and increase in steps of $1 M_{\odot} \text{pc}^{-2}$. The triangles show the positions of the *K* band isophotes (top) and *R* band isophotes (bottom). The inset more clearly shows the relative positions of the dynamical centers. Errorbars span the FWHM beam. The centers all coincide to better than a beam width.

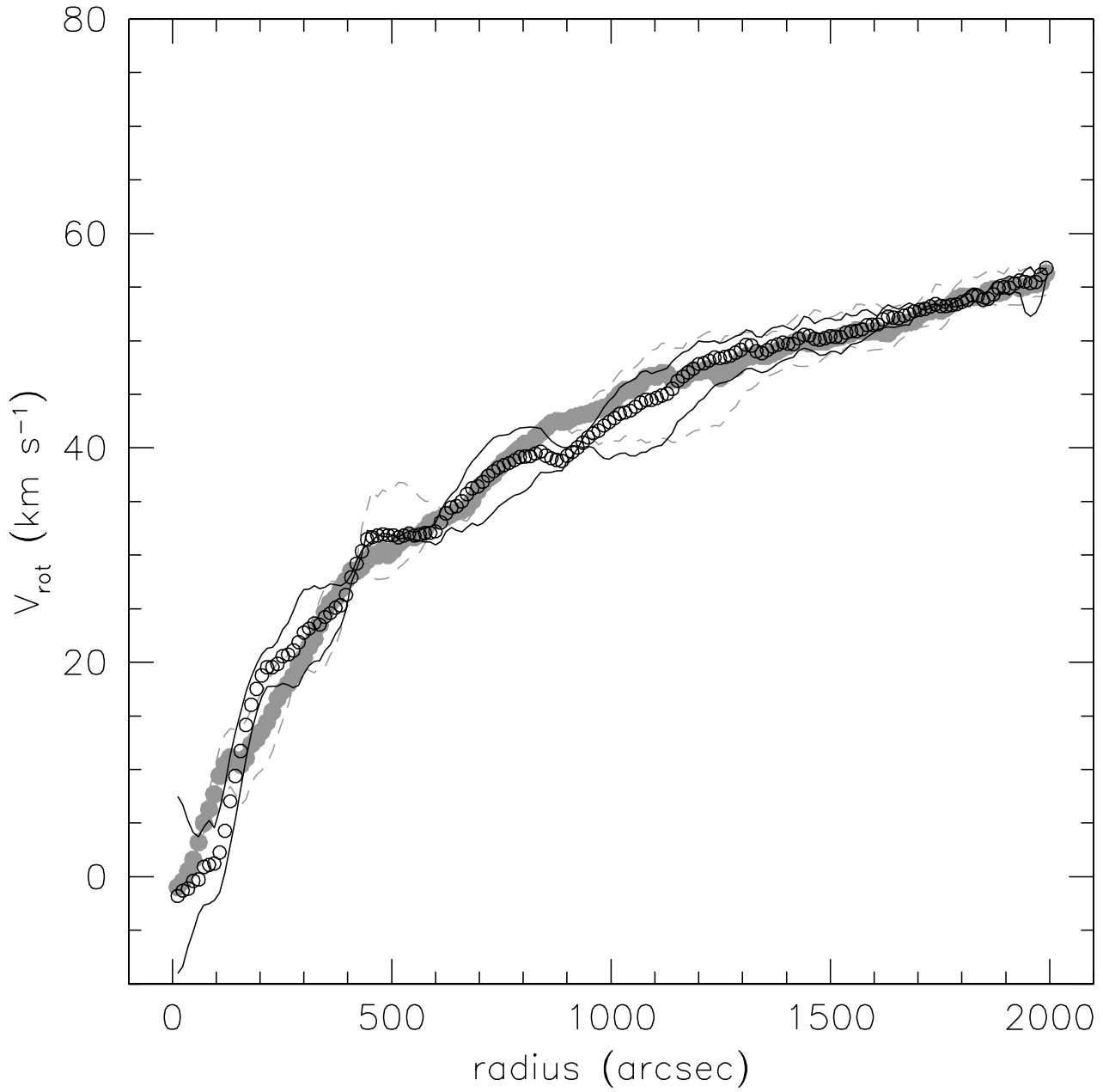


Figure 9. Comparison of the B12 rotation curves derived using the true dynamical center as central position (grey curves), and using the *K*-band optical center as central position (black curves). The thin lines represent the curves from the approaching and receding sides separately.

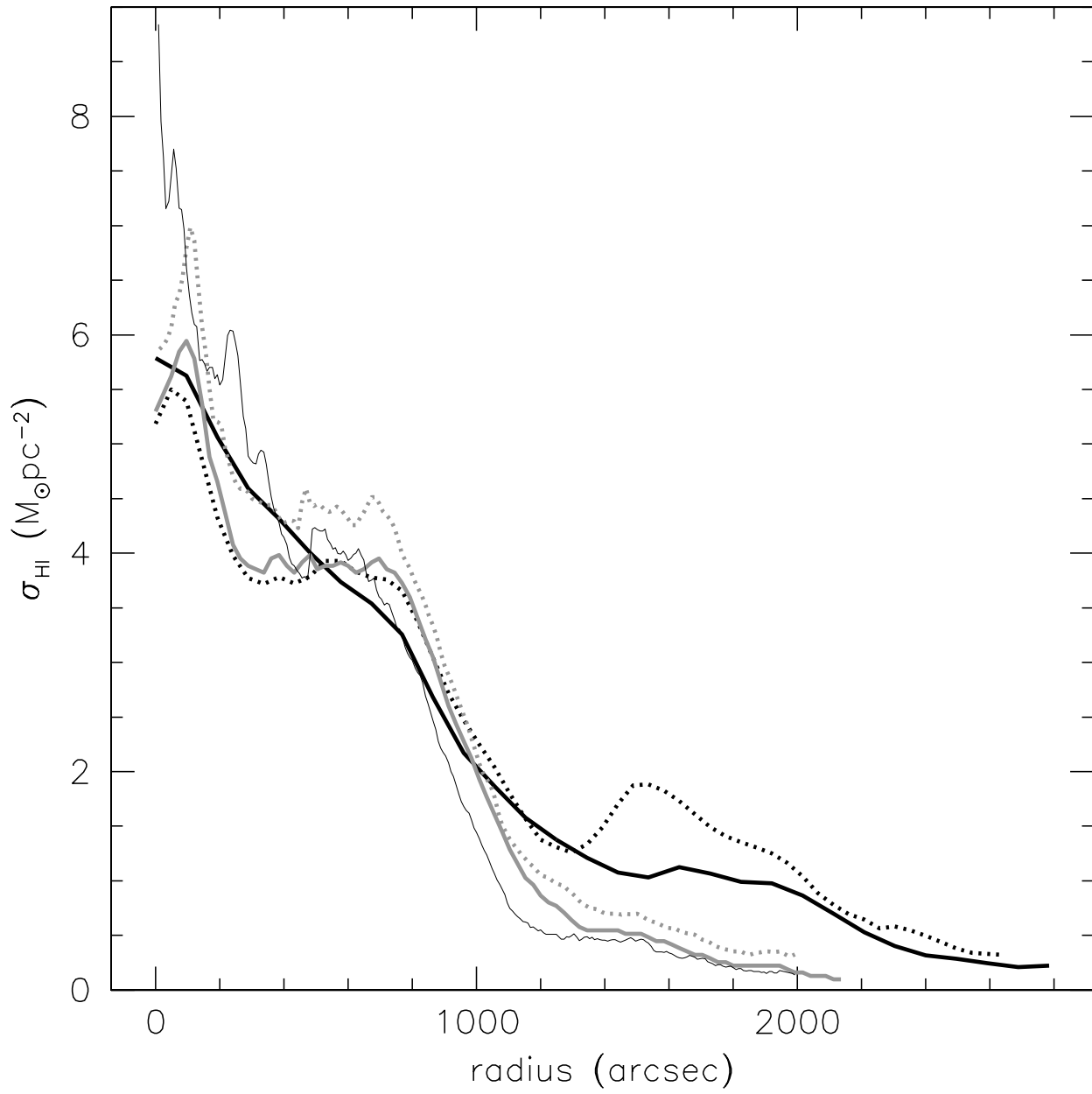


Figure 10. HI surface density profiles, corrected for inclination. The various resolutions are distinguished as follows: B96: full thick black line; B48: dotted thick black line; B24: full grey thick line; B12: dotted grey thick line; B08: full thin black line.

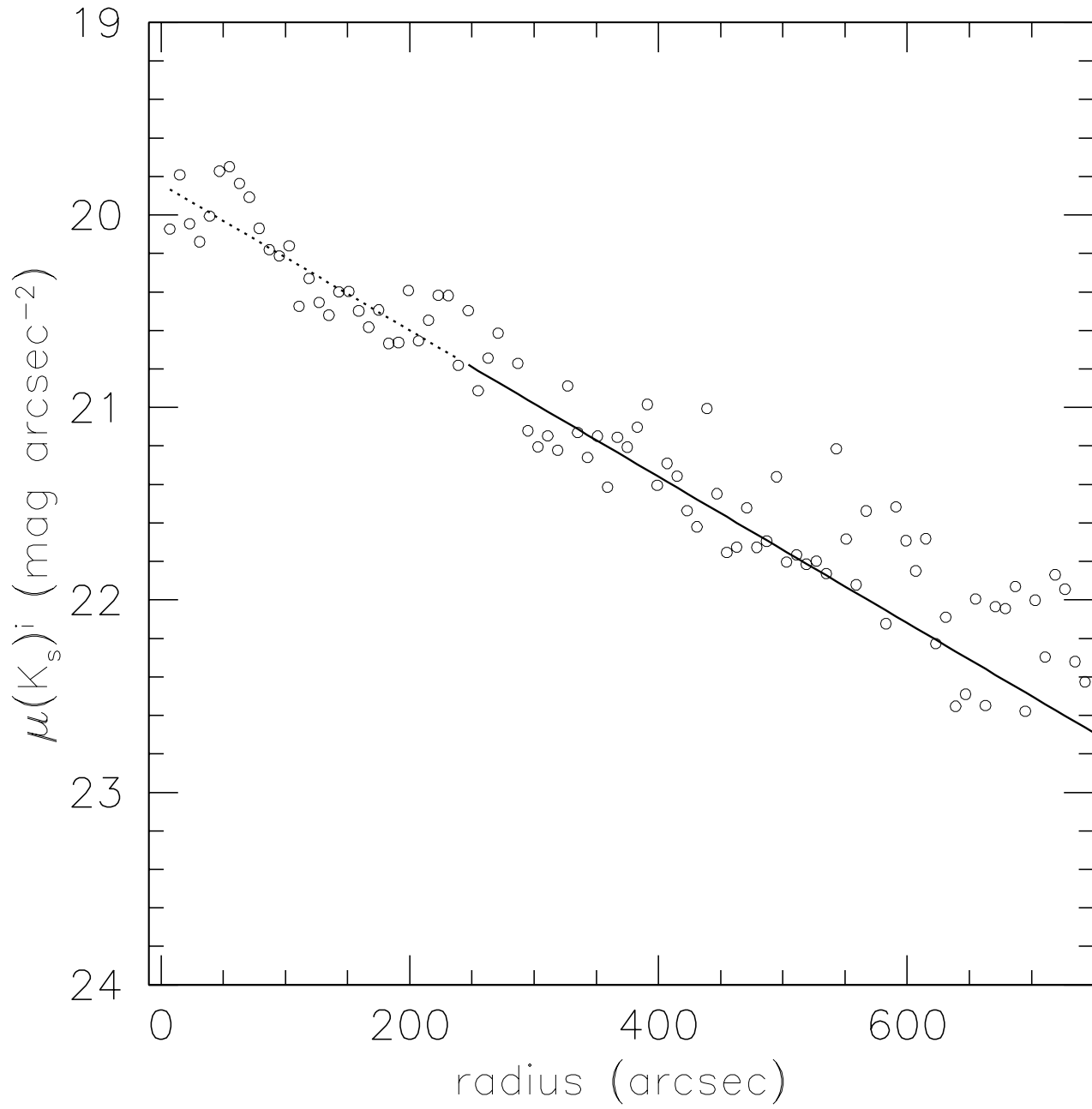


Figure 11. Azimuthally averaged K -band surface brightness profile. The profile is corrected for inclination and Galactic foreground extinction. Spacing between the points is $8''$. The line indicates the exponential disk fit used at radii $R > 240''$.

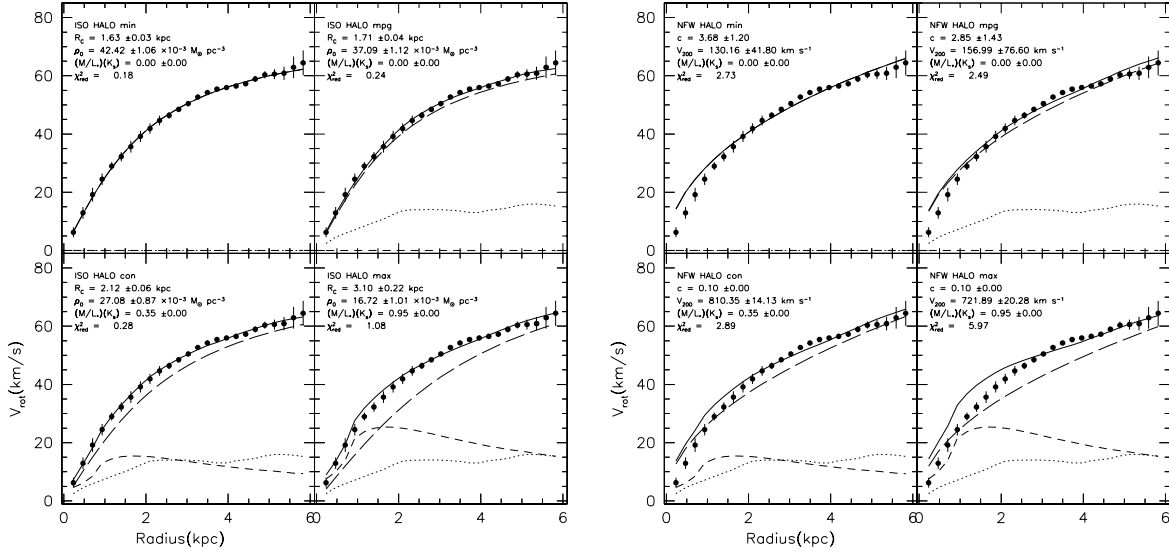


Figure 12. B96 mass models. The left column shows the fits made using a pseudo-isothermal (ISO) halo. The right column shows the NFW halo fits. The top row shows fits made to the entire rotation curve, while the bottom row shows fits to the inner curve ($R < 1000''$). In each panel the following fits are shown: minimum disk (top-left), minimum disk+gas (top-right), constant Υ_* (bottom-left), and maximum disk (bottom-right). Fit parameters are given in the sub-panels. An error of “0.00” indicates that this parameter was fixed during the fitting.

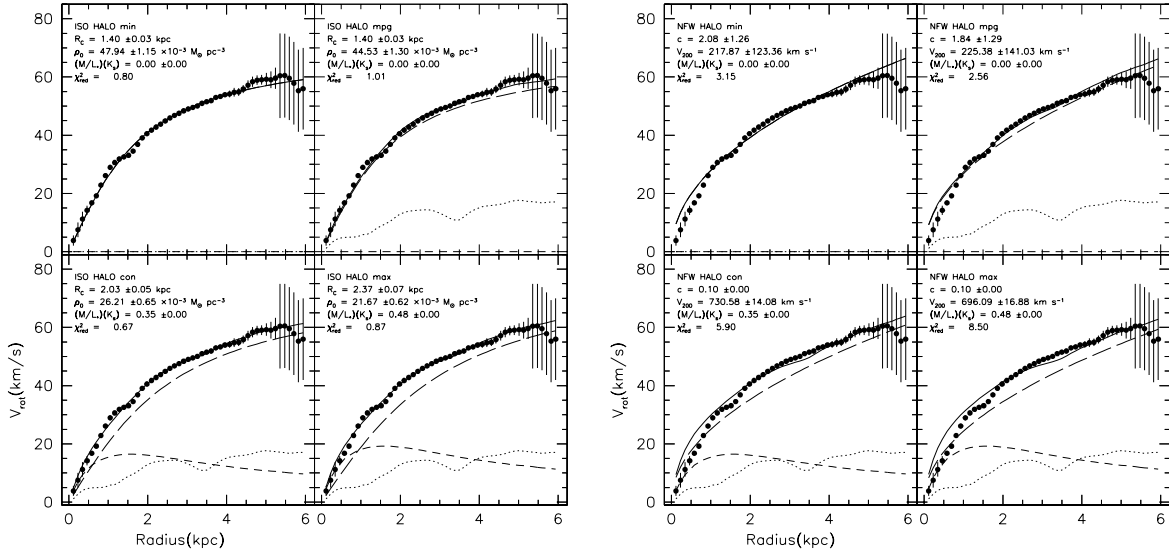


Figure 13. B48 mass models. See Fig. 12.

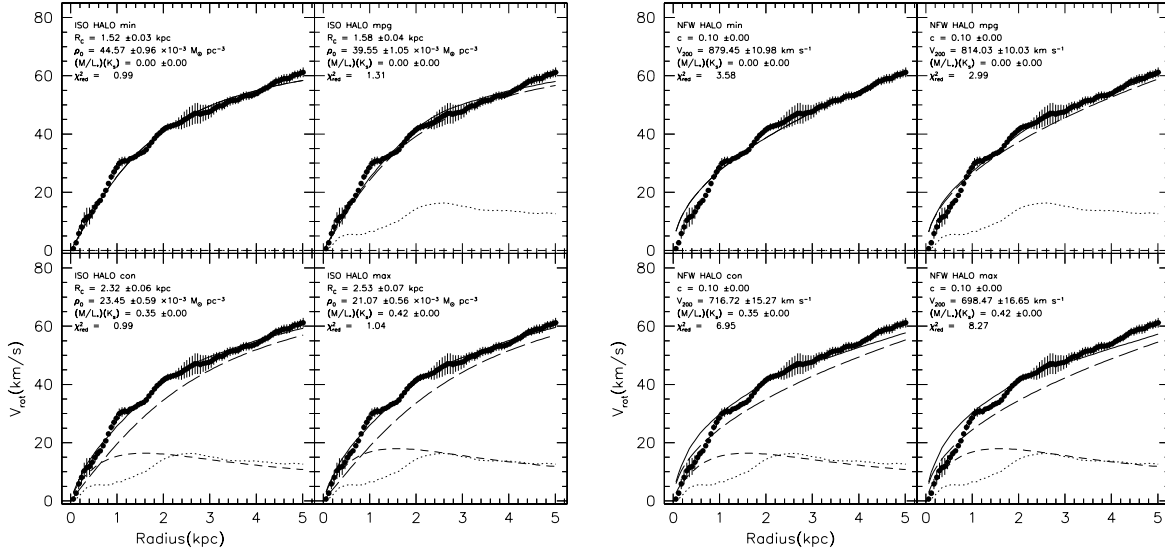


Figure 14. B24 mass models. See Fig. 12.

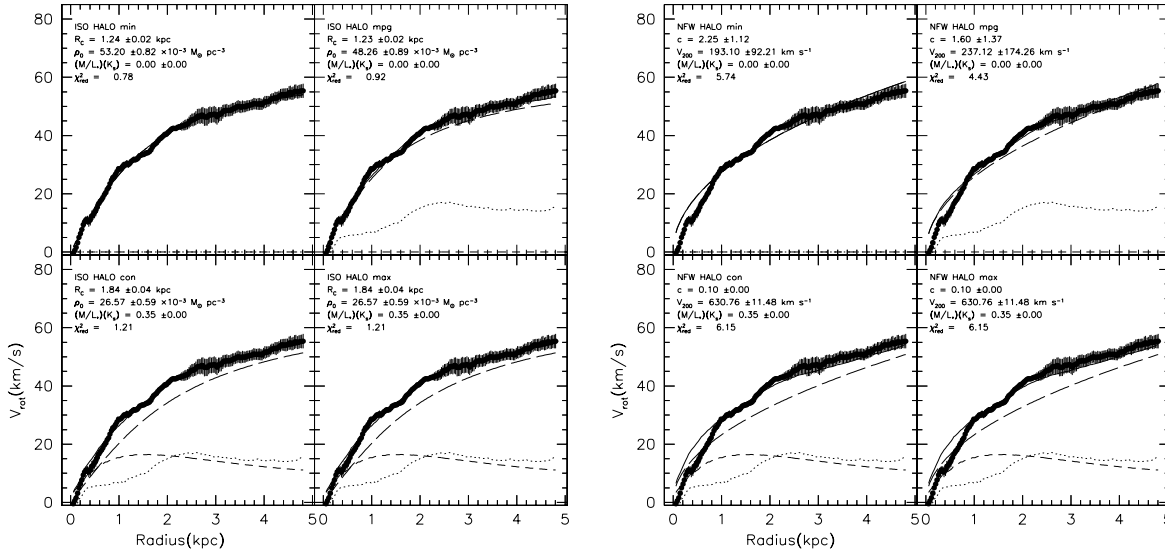


Figure 15. B12 mass models. See Fig. 12.

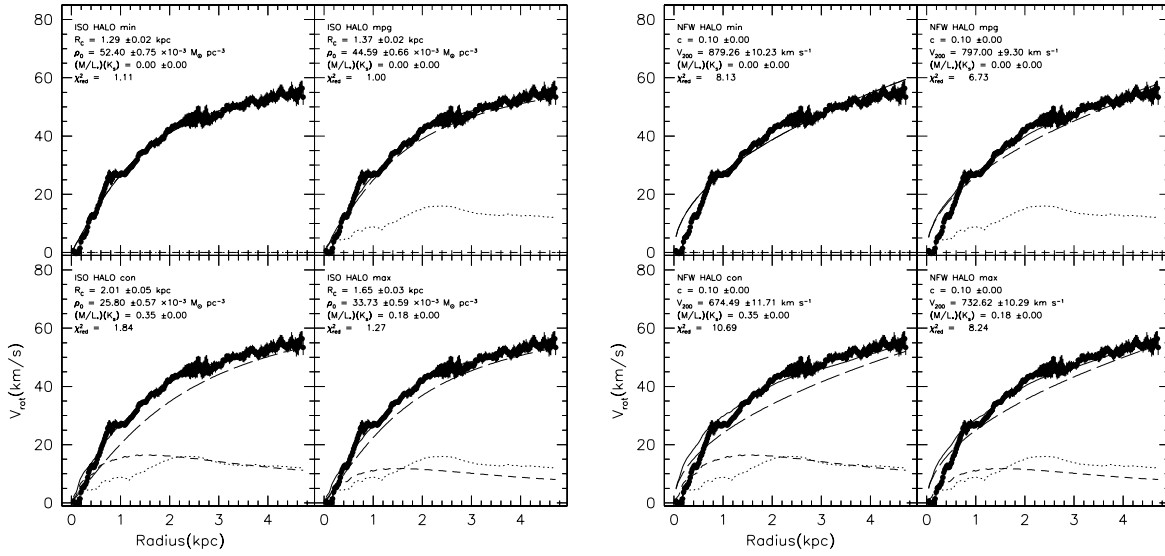


Figure 16. B08 mass models. See Fig. 12.

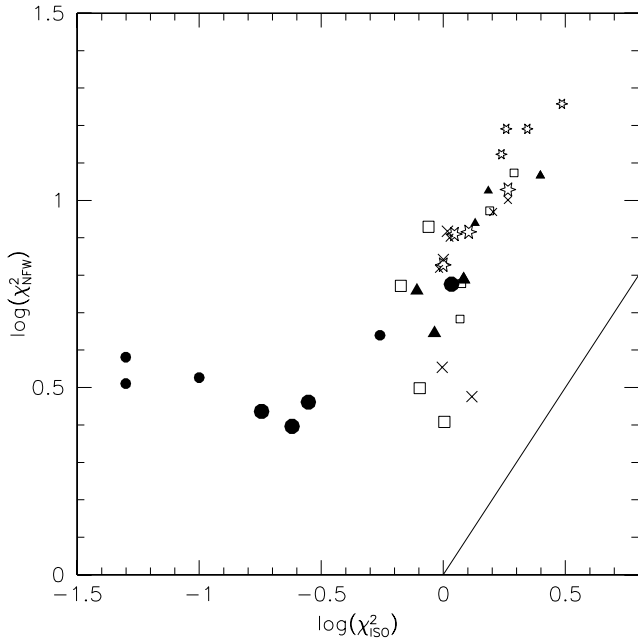


Figure 17. Reduced chi2 plot, $\chi^2(ISO) < \chi^2(NFW)$ at all resolutions and Υ_* . The line is the line of equality. Large symbols represent the fits to the complete curves, small symbols fits to the inner curves. Filled circles: B96; open squares: B48; crosses: B24; filled triangles: B12; and stars: B08.

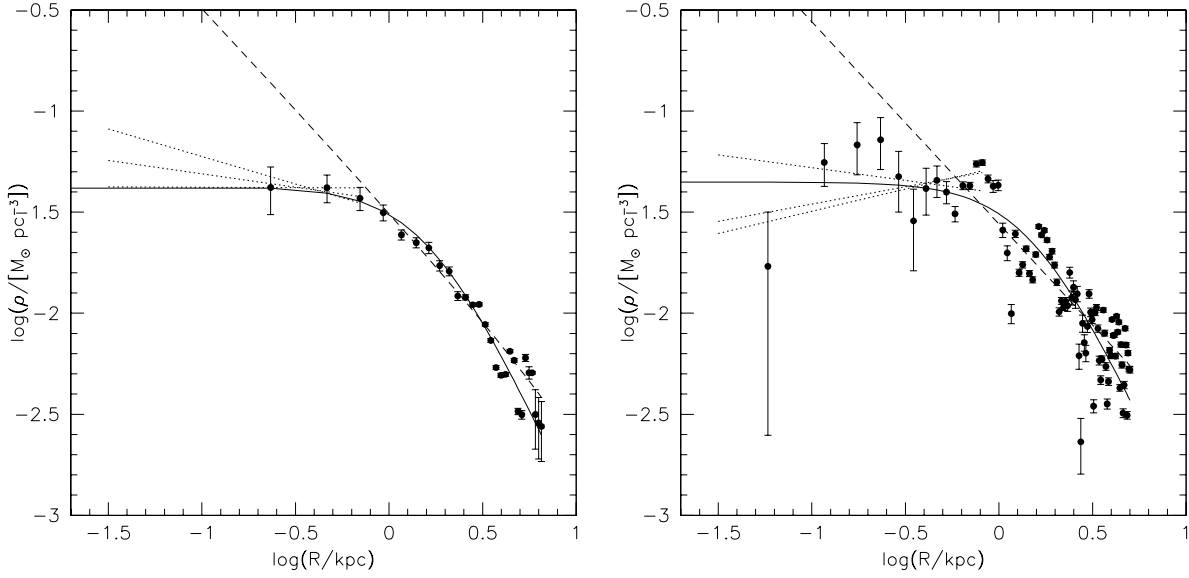


Figure 18. Mass-density profiles for the B96 (left) and B24 (right) models. The long-dashed lines shows the best-fitting minimum disk NFW model, the full line the best-fitting ISO model. The dotted lines represent the power-law fits to the data at $R < 0.8$ kpc.

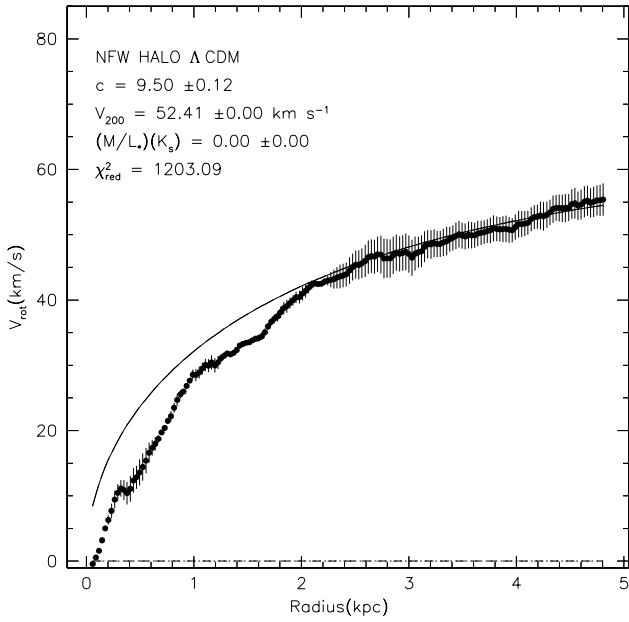


Figure 19. Minimum disk halo for B12 using parameters as required by CDM simulations assuming that $V_{\text{max}} = V_{200}$.

Table 5. Inner mass density slopes

Resolution	α	$\Delta\alpha$
B96	-0.13	0.14
B48	+0.02	0.12
B24	+0.22	0.35
B12	-0.04	0.09
B08	-	-

Table 1. Data cube properties

	B96	B48	B24	B12	B08
beam size (")	349.4 × 96	174.7 × 48	86.4 × 24	42.4 × 12	28.3 × 8
pixel size (")	32 × 32	16 × 16	8 × 8	4 × 4	2.5 × 2.5

All data cubes presented here have a channel separation of 1.6 km s⁻¹, and an effective velocity resolution of 1.9 km s⁻¹.

Table 2. Adopted ROTCUR parameters

	B96	B48	B24	B12	B08
XPOS	19 ^h 44 ^m 57.54 ^s	19 ^h 44 ^m 58.76 ^s	19 ^h 44 ^m 58.71 ^s	19 ^h 44 ^m 58.04 ^s	19 ^h 44 ^m 58.91 ^s
YPOS	-14°49 ^m 13.0 ^s	-14°49 ^m 17.6 ^s	-14°49 ^m 21.7 ^s	-14°49 ^m 18.9 ^s	-14°49 ^m 23.8 ^s
VSYS	-53.3 km s ⁻¹	-54.7 km s ⁻¹	-54.7 km s ⁻¹	-54.4 km s ⁻¹	-54.6 km s ⁻¹
PA	<i>0-1248: 109°</i> <i>1344-2592: 109-138°</i>	<i>0-480: 127-105°</i> <i>480-2400: 105-130°</i>	<i>0-480: 130-105°</i> <i>480-2136: 105-131°</i>	<i>0-456: 140-103°</i> <i>456-1992: 103-130°</i>	<i>0-480: 150-106°</i> <i>480-680: 106°</i> <i>688-1992: 106-130°</i>
INCL	58.7°	59.9°	58.7°	<i>0-1056: 58°</i> <i>1056-1992: 58-68°</i>	<i>0-1096: 57°</i> <i>1104-1992: 57-68°</i>

Italics indicate a range in radius in arcseconds. The pair of numbers following it indicate the linear range in parameter over this radial range.

Table 3. NFW Rotation curve fits

Resolution	model	c	Δc	V_{200}	ΔV_{200}	Υ_*	χ_{red}^2
B96	min	3.7	1.2	130.2	41.8	0	2.73
	mpg	2.8	1.4	157.0	76.6	0	2.49
	con	0.1	...	810.3	14.1	0.35	2.89
	max	0.1	...	721.9	20.3	0.95	5.97
B96 inner	min	0.1	...	878.0	61.6	0	3.81
	mpg	0.1	...	1791.7	56.7	0	3.24
	con	0.1	...	636.9	57.8	0.35	3.36
	max	0.1	...	377.5	65.7	0.95	4.36
B48	min	2.1	1.3	217.9	123.4	0	3.15
	mpg	1.8	1.3	225.4	141.0	0	2.56
	con	0.1	...	730.6	14.1	0.35	5.91
	max	0.1	...	696.1	16.9	0.48	8.50
B48 inner	min	0.1	...	899.6	26.4	0	5.99
	mpg	0.1	...	826.8	23.6	0	4.82
	con	0.1	...	633.6	33.0	0.35	9.38
	max	0.1	...	563.2	37.1	0.48	11.84
B24	min	0.1	...	879.5	11.0	0	3.58
	mpg	0.1	...	814.0	10.0	0	2.99
	con	0.1	...	716.7	15.3	0.35	6.95
	max	0.1	...	698.5	16.7	0.42	8.27
B24 inner	min	0.1	...	876.5	27.2	0	7.95
	mpg	0.1	...	795.1	24.7	0	6.56
	con	0.1	...	591.3	29.4	0.35	9.31
	max	0.1	...	551.1	30.5	0.42	10.02
B12	min	2.3	1.1	193.1	92.2	0	5.74
	mpg	1.6	1.4	237.1	174.3	0	4.42
	con	0.1	...	630.8	11.5	0.35	6.15
	max	0.1	...	630.8	11.5	0.35	6.15
B12 inner	min	0.1	...	889.3	19.2	0	10.61
	mpg	0.1	...	792.0	17.4	0	8.69
	con	0.1	...	592.4	20.1	0.35	11.65
	max	0.1	...	592.4	20.1	0.35	11.65
B08	min	0.1	...	879.3	10.2	0	8.13
	mpg	0.1	...	797.0	9.3	0	6.73
	con	0.1	...	674.5	11.7	0	10.69
	max	0.1	...	732.6	10.3	0.18	8.24
B08 inner	min	0.1	...	898.7	20.6	0	15.52
	mpg	0.1	...	792.7	19.0	0	13.28
	con	0.1	...	590.7	22.3	0.35	18.11
	max	0.1	...	688.2	20.6	0.18	15.52

“min”: minimum disk; “mpg”: minimum disk+gas; “con”: constant Υ_* ; “max”: maximum disk. Dots (...) indicate the parameter was fixed during fitting.

Table 4. ISO Rotation curve fits

Resolution	model	R_C	ΔR_C	ρ_0	$\Delta\rho_0$	Υ_*	χ_{red}^2
B96	min	1.63	0.03	42.4	1.1	0	0.18
	mpg	1.71	0.04	37.1	1.1	0	0.24
	con	2.12	0.06	27.1	0.9	0.35	0.28
	max	3.10	0.22	16.7	1.0	0.95	1.08
B96 inner	min	1.50	0.05	45.0	1.2	0	0.05
	mpg	1.47	0.05	41.3	1.2	0	0.05
	con	2.10	0.17	26.4	1.2	0.35	0.10
	max	∞	...	11.2	0.7	0.95	0.55
B48	min	1.40	0.03	47.9	1.2	0	0.80
	mpg	1.40	0.03	44.5	1.3	0	1.01
	con	2.03	0.05	26.2	0.7	0.35	0.67
	max	2.37	0.07	21.7	0.6	0.48	0.87
B48 inner	min	1.22	0.06	53.5	2.6	0	1.19
	mpg	1.12	0.06	53.3	2.9	0	1.17
	con	1.89	0.21	27.2	2.0	0.35	1.55
	max	2.70	0.55	20.3	1.7	0.48	1.95
B24	min	1.51	0.03	44.6	1.0	0	0.99
	mpg	1.58	0.04	39.5	1.0	0	1.31
	con	2.32	0.06	23.4	0.6	0.35	1.00
	max	2.53	0.07	21.1	0.6	0.42	1.04
B24 inner	min	1.31	0.07	49.8	2.1	0	1.06
	mpg	1.20	0.06	48.7	2.2	0	0.96
	con	2.27	0.34	24.1	1.7	0.35	1.60
	max	2.88	0.65	20.6	1.6	0.42	1.84
B12	min	1.24	0.02	53.2	0.8	0	0.78
	mpg	1.23	0.02	48.3	0.9	0	0.92
	con	1.84	0.04	26.6	0.6	0.35	1.21
	max	1.84	0.04	26.6	0.6	0.35	1.21
B12 inner	min	1.19	0.04	55.0	1.7	0	1.53
	mpg	1.06	0.04	54.4	1.8	0	1.35
	con	1.78	0.15	27.2	1.5	0.35	2.50
	max	1.78	0.15	27.2	1.5	0.35	2.50
B08	min	1.29	0.02	52.4	0.8	0	1.11
	mpg	1.37	0.02	44.6	0.7	0	1.00
	con	2.01	0.05	25.8	0.6	0.35	1.84
	max	1.66	0.03	33.7	0.6	0.18	1.27
B08 inner	min	1.43	0.05	49.0	1.2	0	1.81
	mpg	1.39	0.05	44.3	1.3	0	1.73
	con	3.01	0.40	22.2	1.0	0.35	3.06
	max	1.88	0.11	31.5	1.1	0.18	2.21

“min”: minimum disk; “mpg”: minimum disk+gas; “con”: constant Υ_* ; “max”: maximum disk.